Enhanced High Q Whispering Gallery Resonator Sensing

by

Wenyan Yu
B.Sc., Zhejiang University, 2006

A Thesis Submitted in Partial Fulfillment of the
Requirements for the Degree of

MASTER OF APPLIED SCIENCE

in the Department of Electrical and Computer Engineering

© Wenyan Yu, 2012
University of Victoria

All rights reserved. This thesis may not be reproduced in whole or in part, by photocopying or other means, without the permission of the author.

Enhanced High Q Whispering Gallery Resonator Sensing

by

Wenyan Yu
B.Sc., Zhejiang University, 2006

Supervisory Committee

Dr. Tao Lu, Supervisor
(Department of Electrical and Computer Engineering)

Dr. Chris Papadopoulos, Departmental Member
(Department of Electrical and Computer Engineering)

Supervisory Committee

Dr. Tao Lu, Supervisor
(Department of Electrical and Computer Engineering)

Dr. Chris Papadopoulos, Departmental Member
(Department of Electrical and Computer Engineering)

ABSTRACT

This thesis presents a novel method to fabricate metallic nanostructures on whispering gallery mode (WGM) cavity surfaces. The unique properties of WGM cavities have shown their promising future in both fundamental research and engineering applications. High sensitivity biosensors are one of the most important applications. Thanks to their ultra high quality factor (Q) and small optical mode volume, the resonant frequency shift of a single nanoparticle binding becomes detectable. The basic principles of a WGM cavity and its coupling mechanism with an optical coupler are discussed in detail. From the WGM sensing principle, people have demonstrated the positive contributions of the surface plasmon to the sensitivity. Furthermore, we implement the localized surface plasmon resonance (LSPR) on the cavity surface by depositing metallic dots. We use the focused ion beam (FIB) to directly deposit metallic nanodots on the spherical cavity surface for the first time. The quality factor of the cavity with metallic dots is above 10^7 in both air and water, which is more than one order larger than other published results. Also, the new method is much more controllable and repeatable than previous methods. It reveals a new fabrication method for potential ultra sensitive sensors based on WGM cavities.

In addition, we offer a new mode solver for the toroidal WGM cavity. The microtoroid is a better platform for further investigation of WGM sensing than the microsphere. By expanding cavity modes to a set of normal fiber modes, we formulate the new mode solver based on simple physical principles. The simulation results of the radiative quality factor based on the new mode solver are presented as well.

Contents

List of Figures

ACKNOWLEDGEMENTS

I would like to thank:

Dr. Tao Lu for his insightful guidance and passion in research to encourage me as my supervisor through the whole project;

Steve Herchack and Xuan Du for their helpful discussion and cheerful cooperation during the past two years;

Dr. Byoung C. Choi and Rennie Gardner for the access to the Electron Beam Lithography and suggestions on fabrication;

Dr. Elaine Humphrey and Adam Schuetze for their help on the advanced microscopy facilities.

DEDICATION

To my parents

and

my wife

Chapter 1

Introduction

1.1 General Introduction

The ability to detect a single nanoparticle is desirable for sensing applications. For diagnostic assessments, doctors can diagnose at a much earlier stage, perhaps even before the symptoms develop, allowing for more time and chances to save peoples' lives. Moreover, for lab experiments, it frees the scientists from the collection and purification of sample pieces to focus on the key part, especially important for rare specimens. Currently, most detection methods are based on chemical reactions or labeling to amplify the detection signal, which is costly, time-consuming, and requires complex equipment. There is an alternative way to amplify the signal optically with a microcavity. The detection limit in an aqueous environment is down to a single 12.5 nm radius nanoparticle, and a single influenza A virion has been detected with optical cavities [1]. The advantages of this sensing mechanism, such as being label free, real time and low cost, offer a solution to the potential sensing requirements for daily health care and quick testing. Furthermore, it minimizes the affect to the analyte.

Being different from the traditional Fabry-Pérot cavity [2], the optical microcavity discussed here can keep the light circulating inside due to total internal reflection (TIR) at the interface between the dielectric microcavity and the surroundings [3]. The light resonates near the cavity surface in the Whispering Gallery Modes (WGM) [4]. Similar to its acoustic equivalent, the light confined by such a cavity, such as a dielectric sphere or disk, propagates with little energy loss that leads to the long photon life time and ultra high quality factor ($Q > 10^8$) [5–8]. It is also well

known that the TIR leads to an evanescent field outside of the dielectric boundary [9]. When the wavelength-linearly-swept laser from a tunable laser enters and exits the cavity through an evanescent waveguide coupler, its transmission spectrum displays a Lorentzian dip at resonance. Here the laser wavelength at the dip coincides with the resonance wavelength of the cavity and equals an integer fraction of the optical path that the photon travels per round trip. The linewidth of this dip is inversely proportional to the quality factor, or equivalently, the expected lifetime of the photon inside the cavity. Upon the presence of a small particle on the cavity surface, the photon that sees the particle will travel an extra distance, increasing the resonance wavelength of the cavity. Therefore, by monitoring the resonance wavelength shift from the observation of the location change of the Lorentzian dip, one is able to detect the single nanoparticle binding event. The sensitivity of this detection technique is comparable to the linewidth of the lorentz dip or, equivalently, the quality factor of this resonator.

An alternative sensing technique is attained by exploiting the surface plasmon resonance (SPR) at the interface of metal and dielectric medium excited by the TIR [10–13]. The physical principle under the SPR is as follows [14]. The surface plasmon wave can be excited at the interface of metals and dielectrics optically, when the frequency of the incident light matches the natural frequency of the electron oscillation at the metal surface. Like the evanescent field, this wave decays exponentially to both mediums, but most of the field concentrates in the dielectric material. A specific incident light can satisfy the frequency match condition by changing its incident angle. So it is used for gas or bio-particle detection by scanning the wavelength at a fixed angle, or alternatively scanning the light incident angle at a fixed wavelength. When the surface plasmon resonance is confined in a metallic nanostructure, it is called localized surface plasmon resonance (LSPR), which is not sensitive to the angle of incident light.

One common obstacle with LSPR is that its sensitivity is limited by the strong energy loss, compared with the WGM cavity, and the less chances for the photon to interact with the adhered analyte particle [15]. The SPR mode coupled from the exciting light can enhance the evanescent field greatly [16], although the metal causes some extra loss of the field. The enhanced evanescent field due to the SPR can increase the resonant frequency shift of the binding, if one implements the LSPR effect properly on a WGM cavity without destroying the quality factor too much.

The motivation of this work is to combine benefits of the high quality factor of

WGM cavities with the strong evanescent field from SPR. The improvement of the WGM sensitivity is achievable with the ratio of the larger frequency shift with respect to the affordable resonant frequency broadening. Some pioneering works attempt to grow some metallic nanoparticles on the dielectric surface of a WGM cavity [17, 18]. An enhancement factor around 4 of the frequency shift is achieved at the cost of greatly reducing the quality factor down to 5×10^5 [19]. In this thesis, we fabricate the metallic nanostructures precisely on the WGM cavity surface for the first time with focused ion beam (FIB). The quality factor of this cavity is higher than 2×10^7 in air and maintains $(1.4 \pm 0.1) \times 10^7$ in the aqueous environment.

1.2 Thesis Outline

Chapter 2 provides the basic theory of the WGM cavity. Some important related concepts, such as the quality factor, loss mechanism and optical mode volume, are included as well.

Chapter 3 demonstrates the coupling and extraction of light for a WGM cavity. We focus on the interaction between a fiber taper and the cavity.

Chapter 4 illustrates a new mode solver for the microtoroid cavity, which is important for the future investigation on the more ideal WGM platforms. This method can be readily transferred to all the axial symmetric WGM cavities.

Chapter 5 depicts the experimental fabrications and measurements performed. Most of the results and analysis are based on the microsphere cavities.

Chapter 6 concludes the thesis and the main contributions to the area.

Chapter 2

Background

Optical microcavity is increasingly attractive for both of the scientists and engineers due to its inherent low optical loss and the capability to confine light into a small volume over a long period [4, 20, 21]. Similar to the sound wave traveling within the gallery of St. Paul's Cathedral in London with so little dissipating that the whisper can be heard by some one far away on the opposite side [22], the light kept in the microcavity resonator is excited in the Whispering Gallery Mode (WGM) with little energy loss per resonant cycle [7]. The atomic smooth surface due to the surface tension of such kind of cavity is the key role for continuous total internal reflections on the interface to ensure the WGM formed inside the cavity [23]. The WGM enables the microcavity to be suitable for some applications such as high sensitive biological and chemical sensors [24–26], nonlinear optical interactions [6, 27] and a powerful tool for fundamental research like cavity quantum electrodynamics (CQED) [28, 29]. The desirable properties of microcavity such as low cavity loss, small mode volume and the high coupling efficiency are critical to the enhanced interaction between the atom and the development of electromagnetic (EM) field [30, 31]. Besides, with the high amplified circulating optical power inside a small volume, it is easy for such cavity to observe the nonlinear optical effects with low threshold power, such as multi-order Raman lasing [32, 33].

2.1 Quality Factor

The quality factor Q is a basic dimensionless parameter widely used to characterize the resonators [3]. A resonant system with a higher quality factor has a lower rate of

energy loss during each oscillation. This factor is defined to be the product of 2π and the ratio of total stored energy in a cavity to the energy loss during a single resonant cycle. According to the definition, the Q of a WGM cavity is inversely proportional to its energy loss. Equivalently, we write it with the total stored energy E_{stored} and loss power P_{loss} as

$$Q = 2\pi f_r \times \frac{E_{stored}}{P_{loss}} = \omega_r \tau. \tag{2.1}$$

Here, f_r is the resonant frequency of the cavity, ω_r is the resonant angular frequency and τ is the life time for the light circulating within an optical cavity before its escaping. Thus, measuring the life time is one of the techniques people used to measure the quality factor of an optical cavity [6].

For a typical ultra high Q microcavity, which has a quality factor of 100 million, excited by a 600 nm laser, one can work out the corresponding life time of a photon traveling inside the cavity, $\tau \approx 3 \times 10^{-8}$ s. As the photon travels at a speed of $v \approx c/n$ where n is the refractive index of the cavity, it can circulate in the cavity for several meters before escaping. Equivalently, it can circulate along the edge of the WGM cavity for about ten thousand round trips and sample any small particles or atoms for the same number of times, causing noticeable changes of the optical properties of the cavity. Therefore, by monitoring the changes of the cavity optical properties such as resonance wavelength shift, one can use such ultra-high Q cavity as an unique highly sensitive nanodetector.

In general, the total quality factor Q_{total} of a WGM cavity can usually be considered to be composed of the intrinsic quality factor $Q_{intrinsic}$ and the coupling quality factor $Q_{coupling}$ [7]. They satisfy the relation according to the Eq. (2.2)

$$\frac{1}{Q_{total}} = \frac{1}{Q_{intrinsic}} + \frac{1}{Q_{coupling}}, \tag{2.2}$$

where the $Q_{intrinsic}$ characterizes the energy loss due to microcavity itself and the $Q_{coupling}$ arises the energy loss during the coupling of the light into and/or out of the microcavity. The intrinsic quality factor can be further separated into four independent terms according to their origins and related by

$$\frac{1}{Q_{intrinsic}} = \frac{1}{Q_{mat}} + \frac{1}{Q_{rad}} + \frac{1}{Q_{ss}} + \frac{1}{Q_{contam}}, \tag{2.3}$$

where the Q_{mat} represents the material loss due to the light absorption by cavity

material and is also defined as bulk loss Q_b; the Q_{rad} represents the radiation loss caused by the Whispering Gallery Mode, also called as Q_{WGM}; the third part Q_{ss} is named for the scattering loss as a result of the imperfection of the microcavity surface; and the Q_{contam} represents the optical loss because of the contaminants attached on the microcavity surface such as H_2O and it is also called as surface adsorption loss Q_{sa}.

Among them, Q_{mat}, Q_{rad} and $Q_{coupling}$ are typically dominant. In addition, they are the basic optical loss mechanisms for understanding the physics under the interesting phenomenon of the WGM microcavity. One can reduce the loss from the contamination on cavity surface by making and keeping the cavities in a clean or vacuum environment. Researchers found that the recorded Q will drop by 20% in the first five minutes after the fabrication [7] before it reaching the saturation state gradually in the next a few hours. The first stage of the contamination is the fast adsorption of oxygen and water molecule from the atmosphere. A layer of OH groups are formed and bonded on the fresh silica surface chemically. Baking the cavity can partially recover the Q. Since the OH groups has a strong absorption only in the infrared region, one can avoid its contribution by choosing other light sources. For our microsphere samples, they maintain the quality factor above 100 million in air at 630 nm wavelength for a few weeks. The surface scattering loss can be calculated with the similar methods as that developed earlier for the planar optical waveguide [23],

$$Q_{ss} \simeq \frac{3\lambda^2 l^{10/3}}{16\pi^5 \sigma^2 n^2 q^{5/2}}. \tag{2.4}$$

Here, σ is the mean size of the inhomogeneities, n is the refractive index which is 1.4457 for silica, $l = \pi D n/\lambda$ is the azimuthal mode order and q is the radius mode order. For a regular glass surface $\sigma = 50$ nm [23], while this is reduced to smaller than 2 nm for the surface tension induced cavity surface [6]. We plot the estimated Q_{ss} of both in Fig. 2.1 for cavities with different sizes. Generally speaking, the cavities with reflowed surface hold a three orders higher quality factor than that with regular glass surface for same size. As in our experiments, the cavity size is lager than 60 μm in diameter. From Fig. 2.1, we also point out that the Q_{ss} beyond this size is higher than 10^{10} which is above the present Q records for the silica fused microcavity [7]. So, the surface scattering loss is not the limiting factor to get a high Q cavity. Here we consider the material absorption, the radiation and coupling loss as the crucial components of the total quality factor.

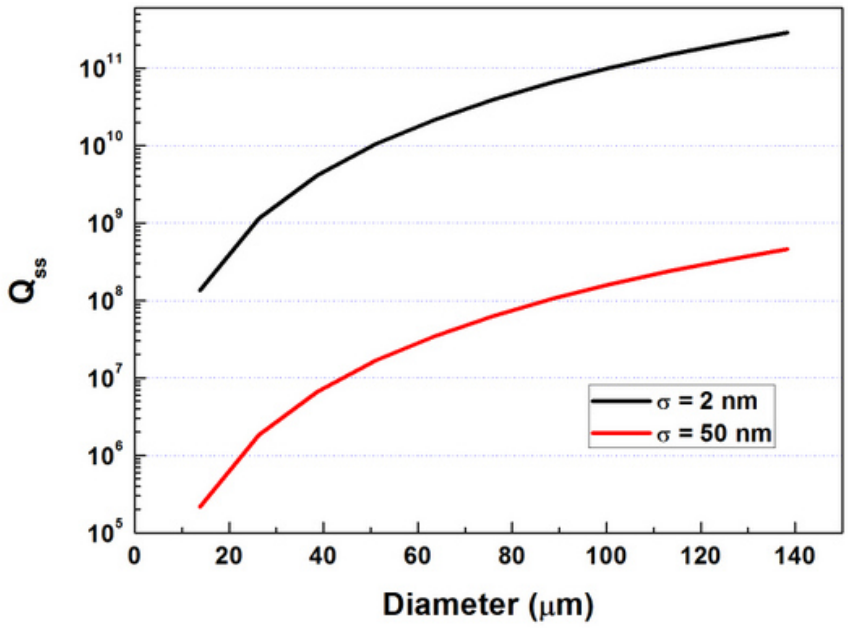

Figure 2.1: Illustration of the estimated quality factors from surface scattering loss for microcavities with different sizes at 630 nm wavelength. The red one is for the regular glass surface. The black one represents the reflowed silica surface which is roughly three orders better than that without reflow. It shows that the surface tension does reduce the surface scattering loss significantly.

2.2 Silica Fused Cavities

There are several different types of WGM optical microcavities, including microsphere, microdisk and microtoroid. People first observed the optical WGM phenomenon in a liquid droplet [34], but the Q is relatively low which is below 10^6. Inspired by that, it is natural to change the medium to a solid dielectric transparent material that has a more stable structure and a much lower absorption to the light. Braginsky et al. [23] first demonstrated the high Q microsphere ($Q \simeq 10^8$) in 1989, and later they improved it to $Q = (0.8 \pm 0.1) \times 10^{10}$ [7], the highest record for silica microsphere up to date. The microsphere, shown in micrograph from Fig. 2.2, is formed on an optical fiber tip with a stem to support it. Here, a miniature oxygen-hydrogen flame or high power CO_2 laser is used to reflow the fiber tip. Due to the induced surface tension, a transparent cavity with smooth surface and spherical shape is formed when the melted glass cools down. Consequently, the surface scattering loss

is reduced significantly, making the Q_{ss} high enough to be negligible.

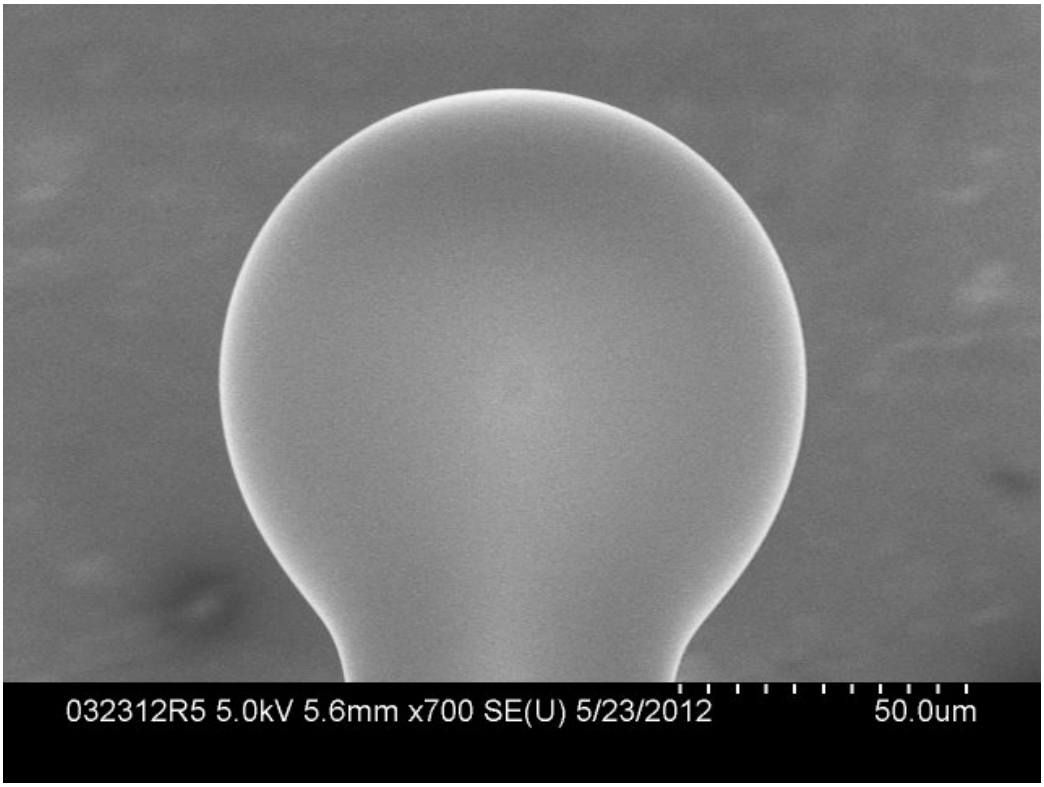

Figure 2.2: A scanning electron microscope (SEM) image of the optical microsphere standing on the fiber stem. The diameter of the microsphere is around 100 μm which is the suitable size for sensing.

Compared with the microsphere, the microdisk (Fig. 2.3) based on silicon-on-insulator (SOI) illustrated in [8] is suffering from the high surface scattering loss due to the etch-induced imperfection on the wall side. Lacking of the reflow process, it yields a relative low quality factor ($Q < 10^6$) for the microdisk until very recently when a new chemical etching method boosted the Q of a microdisk in large diameters ($D \sim 1$ mm) to 10^9 [35]. However, it requires a complex fabrication process. On the other hand, the regular microdisk fabrication process is compatible with the modern standard very large scale integrated circuits (VLSI) procedure and can be integrated with other optical electrical devices on a single chip.

To implement the surface tension and reduce the boundary defects, we reflow the microdisk and get a microtoroid consequently. The microtoroid was first fabricated by Vahala's group at Caltech in 2003 [5]. Fig. 2.4 shows the geometrical shape of a microtoroid on a silicon chip and illustrates the fabrication process from a microdisk.

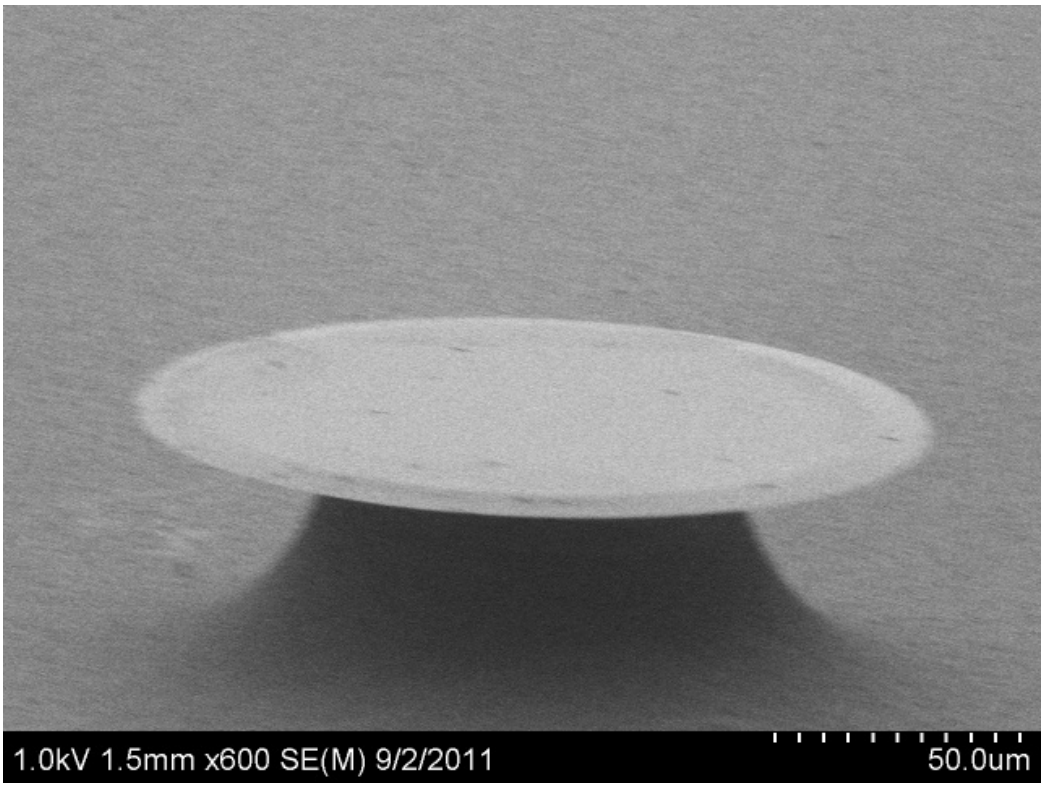

Figure 2.3: A SEM micrograph of the microdisk with diameter around 150 μm on the silicon wafer. The disk is made of silica while the pillar under it is made of silicon.

The microtoroid is fabricated on the silicon wafer covered with a layer of 2 μm thick SiO_2. The disk shaped pattern is created by photolithography, and then the patterned wafer is immersed into the HF solution for etching. After removing the photo-resist with acetone, the XeF_2 is induced for the isotropic removal of silicon, leaving the SiO_2 microdisk overhang on a silicon pillar. The last step is to selectively heat the SiO_2 disk without affecting the silicon. Since the silicon have a far weaker optical absorption near 10.6 μm wavelength and a 100 times higher thermal conductivity, the silicon pillar can remain at the solid state while the disk melting occurs when it is exposed under a CO_2 laser beam. Due to the surface tension during the selectively heating process, the self-smoothing leads to a much smaller surface scattering loss than the microdisk.

Although the microtoroid does not have a Q_{total} as high as that of the microsphere ($Q_{total} \sim 10^9$), the optical fiber based fabrication of the microsphere makes it very difficult and inconvenient for further developing into the chip based devices. Since the microtoroid is fabricated based on a microdisk, it has a more promising future

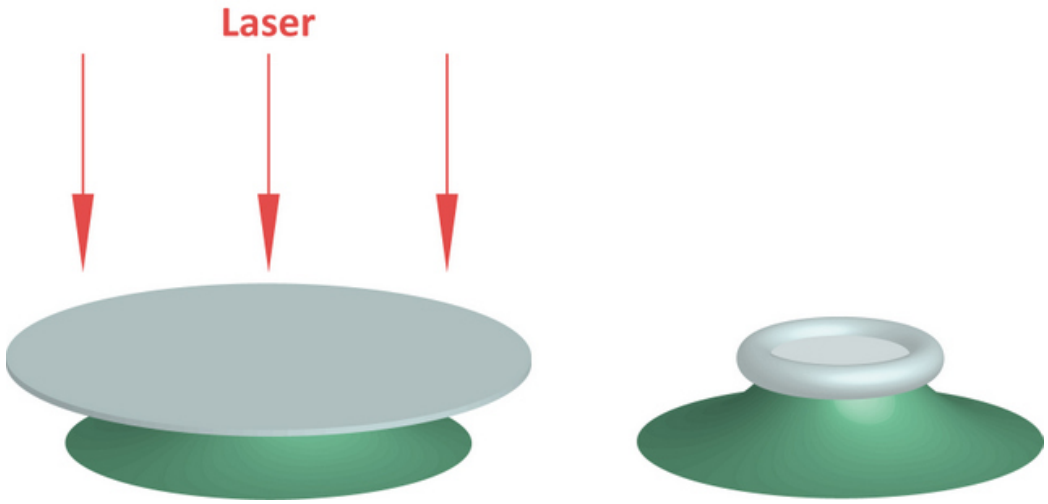

Figure 2.4: The silica disk is fabricated by the standard photolithography procedure, and then the XeF_2 is induced to remove the silicon isotropically while the SiO_2 layer remains. The last step is to selectively heat the SiO_2 disk without affecting the silicon.

in integrating with other optics or electrical devices. Another advantage of the microtoroid is that its fabrication process is self-quenching with the diameter controlled by the lithography and chemical treatment. This makes the microtoroid fabrication more controllable and reproducible than the microsphere.

2.3 Loss Mechanism

This section investigates the electromagnetic (EM) field behaviors inside this system. First consider the Maxwell's equations for a charge and current free dielectrics [9],

$$\nabla \cdot \mathbf{D} = 0, \tag{2.5}$$

$$\nabla \times \mathbf{E} = -\frac{\partial \mathbf{B}}{\partial t}, \tag{2.6}$$

$$\nabla \cdot \mathbf{B} = 0, \tag{2.7}$$

$$\nabla \times \mathbf{H} = \frac{\partial \mathbf{D}}{\partial t}, \tag{2.8}$$

where $\mathbf{D}$ is the electric displacement field, $\mathbf{E}$ is the electric field, $\mathbf{B}$ is the magnetic field and $\mathbf{H}$ is the magnetizing field. When the medium is piece-wise homogeneous, which is true in our case, $\mathbf{D} = \epsilon\mathbf{E}$ and $\mathbf{H} = \frac{1}{\mu}\mathbf{B}$, where $\epsilon = \epsilon_r\epsilon_0$ is the permittivity, ϵ_r is the relative permittivity, ϵ_0 is the permittivity of free space; $\mu = \mu_r\mu_0$ is the

permeability, μ_r is the relative permeability, μ_0 is the permeability of free space. The electromagnetic wave propagates through a piece-wise homogeneous medium at a speed

$$v = \frac{1}{\sqrt{\mu\epsilon}} = \frac{c}{n}, \tag{2.9}$$

where $c = 1/\sqrt{\mu_0\epsilon_0}$ is the speed of light in free space and $n = \sqrt{\mu\epsilon}/\sqrt{\mu_0\epsilon_0} = \sqrt{\mu_r\epsilon_r}$ is the refractive index. Then, applying the curl operator to the curl of the EM field (Eq. (2.6) and Eq. (2.8)), and taking into consideration of Eq. (2.8) and (2.6) respectively, we get[1]

$$\begin{aligned} \nabla \times (\nabla \times \mathbf{E}) &= \nabla(\nabla \cdot \mathbf{E}) - \nabla^2\mathbf{E} = \nabla \times (-\mu\frac{\partial \mathbf{H}}{\partial t}) \qquad (2.10) \\ &= -\mu\frac{\partial}{\partial t}(\nabla \times \mathbf{H}) = -\mu\epsilon\frac{\partial^2 \mathbf{E}}{\partial t^2}, \\ \nabla \times (\nabla \times \mathbf{H}) &= \nabla(\nabla \cdot \mathbf{H}) - \nabla^2\mathbf{H} = \nabla \times (\epsilon\frac{\partial \mathbf{E}}{\partial t}) \qquad (2.11) \\ &= \epsilon\frac{\partial}{\partial t}(\nabla \times \mathbf{E}) = -\mu\epsilon\frac{\partial^2 \mathbf{H}}{\partial t^2}. \end{aligned}$$

Combining with the Eq. (2.5) and (2.7), we decouple the electric field and magnetic field into two separated expressions with the equivalent form. This yields one set of wave equations for the electric field and magnetic field respectively

$$\begin{cases} \nabla^2\mathbf{E} = \mu\epsilon\frac{\partial^2 \mathbf{E}}{\partial t^2} = (\frac{n}{c})^2\frac{\partial^2 \mathbf{E}}{\partial t^2} \\ \nabla^2\mathbf{H} = \mu\epsilon\frac{\partial^2 \mathbf{H}}{\partial t^2} = (\frac{n}{c})^2\frac{\partial^2 \mathbf{H}}{\partial t^2}. \end{cases} \tag{2.12}$$

Looking into the above set of equations, we notice that the left hand side is fields changing with space, while the right hand side is only the evolution of time. We can apply the variable separation method to represent the electric and magnetic fields as below

$$\begin{cases} \mathbf{E} = \mathbf{E}(\mathbf{r}, t) = \mathbf{E}(\mathbf{r})T(t) \\ \mathbf{H} = \mathbf{H}(\mathbf{r}, t) = \mathbf{H}(\mathbf{r})T(t) \end{cases} \tag{2.13}$$

where $\mathbf{E}(\mathbf{r})$ and $\mathbf{H}(\mathbf{r})$ are functions that only dependent on space, and $T(t)$ is a function of time. Substituting the above forms into the wave equations 2.12, we

[1]See details in appendix A.1.

obtain

$$\begin{cases} T(t)\nabla^2\mathbf{E}(\mathbf{r}) = \mathbf{E}(\mathbf{r})(\frac{n}{c})^2\frac{\partial^2 T(t)}{\partial t^2} \\ T(t)\nabla^2\mathbf{H}(\mathbf{r}) = \mathbf{H}(\mathbf{r})(\frac{n}{c})^2\frac{\partial^2 T(t)}{\partial t^2}. \end{cases} \tag{2.14}$$

Next, both sides of the above equations are divided by $\mathbf{E}(\mathbf{r})T(t)$ and $\mathbf{H}(\mathbf{r})T(t)$ respectively, and we find

$$\begin{cases} \frac{\nabla^2\mathbf{E}(\mathbf{r})}{\mathbf{E}(\mathbf{r})} = (\frac{n}{c})^2\frac{1}{T(t)}\frac{\partial^2 T(t)}{\partial t^2} \\ \frac{\nabla^2\mathbf{H}(\mathbf{r})}{\mathbf{H}(\mathbf{r})} = (\frac{n}{c})^2\frac{1}{T(t)}\frac{\partial^2 T(t)}{\partial t^2}. \end{cases} \tag{2.15}$$

Here, varying either the space or time term but keeping the other fixed, the equations should still hold. Therefore, the space and time changing are independent and both of the two sides have to equal to a constant. Further, we assume

$$\frac{1}{T(t)}\frac{\partial^2 T(t)}{\partial t^2} = -\omega^2. \tag{2.16}$$

Then, we have the expressions for EM field which contain two independent variables

$$\begin{cases} \mathbf{E}(\mathbf{r},t) = \mathbf{E}(\mathbf{r})e^{i\omega t} \\ \mathbf{H}(\mathbf{r},t) = \mathbf{H}(\mathbf{r})e^{i\omega t}. \end{cases} \tag{2.17}$$

$\mathbf{E}(\mathbf{r})$ and $\mathbf{H}(\mathbf{r})$ are independent on time which can be derived to the Helmhöltz equations for EM fields

$$\begin{cases} \nabla^2\mathbf{E}(\mathbf{r}) + k^2\mathbf{E}(\mathbf{r}) = 0 \\ \nabla^2\mathbf{H}(\mathbf{r}) + k^2\mathbf{H}(\mathbf{r}) = 0. \end{cases} \tag{2.18}$$

Here, we introduce the propagating constant

$$k = (\frac{n\omega}{c}) = nk_0, \tag{2.19}$$

where $k_0 = \omega/c$ is the wave number of the light in free space and n is the refractive index of the medium. For silica, which is the main medium of our microcavities, $\mu_r = 1$ but the refractive index is actually a complex number [36], where the imaginary part is very small comparing to the real part. Consequently, the complex refractive index should be written as $\tilde{n} = n + j\kappa$, where $n = n(\omega)$ represents the real part and $\kappa = \kappa(\omega)$ represents a small imaginary part. This leads to the fact that the permittivity has to be a complex number as well. According to Eq. (2.9), we rewrite the refractive index

in a more general form,

$$\tilde{n}^2 = (n + j\kappa)^2 = n^2 - \kappa^2 + j2n\kappa = \mu_r\epsilon_r = \epsilon_r = \epsilon' + j\epsilon'', \tag{2.20}$$

where $\epsilon' = n^2 - \kappa^2$ represents the real part of the complex relative permittivity ϵ_r of silica and $\epsilon'' = 2n\kappa$ represents the imaginary part.

2.3.1 Material Loss

The electric power density I in dielectric materials is [37]

$$I = \mathbf{J} \cdot \mathbf{E}, \tag{2.21}$$

where $\mathbf{J}$ is the displacement current density, and $\mathbf{E}$ is electric field. If the silica cavity could be considered as ideal dielectrics which only have displacement current $\mathbf{J}(\omega)$ without free current [38],

$$\mathbf{J}(\omega) = \frac{d\mathbf{D}}{dt} = \epsilon\frac{d(\mathbf{E}(t=0)e^{j\omega t})}{dt} = j\epsilon\omega\mathbf{E}(\omega). \tag{2.22}$$

Using the complex permittivity and substituting into Eq. (2.21), we obtain the power density for a silica cavity to be

$$I = j\omega\epsilon'\epsilon_0|\mathbf{E}(\omega)|^2 - \omega\epsilon''\epsilon_0|\mathbf{E}(\omega)|^2. \tag{2.23}$$

The first term on the right hand side of Eq. (2.23) is a pure imaginary number that contains the phase information of the field and generates the radiation power. The second term, a real number with a negative sign, represents the power decay along the propagation direction due to the intrinsic material absorption and scattering. Eq. (2.23) further indicates that the material power loss is proportional to the imaginary component of the permittivity.

The material loss due to the silica absorption and scattering is very small, this is the reason that silica fiber is widely used for long distance signal transmission in modern days [7]. The power absorption formula is

$$P = P_0e^{-\alpha x}, \tag{2.24}$$

where P_0 is the input power, P is the output power after the absorption, α is the linear

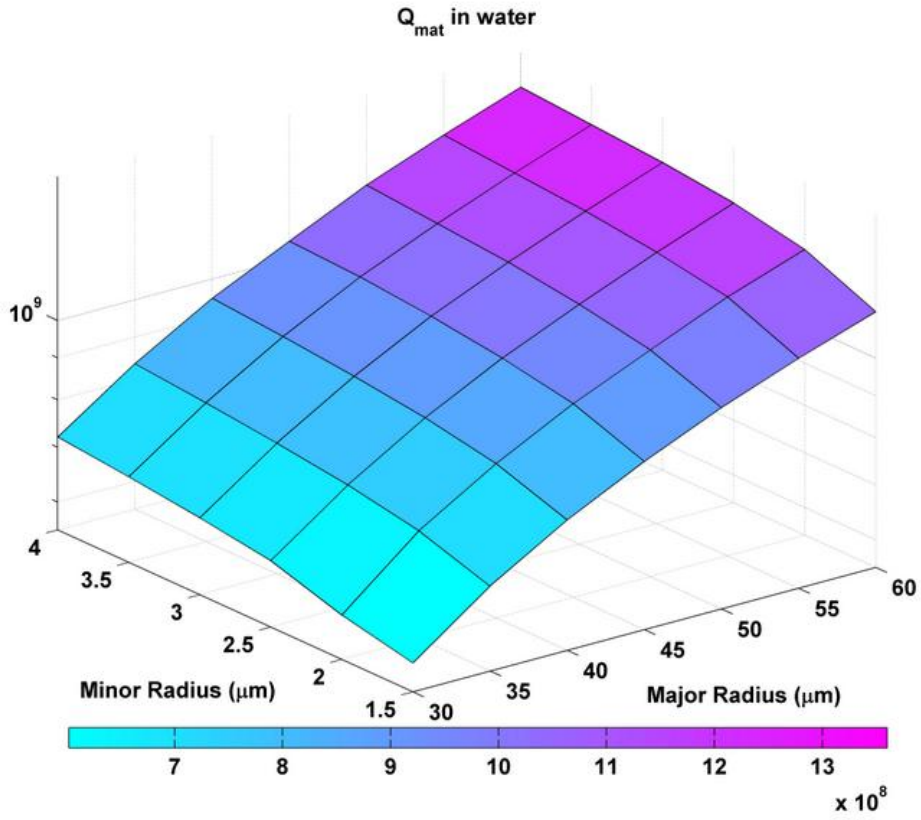

Figure 2.5: The simulation results of the Q_{mat} for microtoroids at 630 nm wavelength in water. The microtoroids with different geometry sizes have different Q_{mat} due to the different mode profiles.

attenuation coefficient in the resonator caused by material and x is the propagating distance. Using the Taylor series, we have $e^{-\alpha x} \simeq 1-\alpha x$ and the power loss $P_0 - P = P_0 \alpha x$. Therefore, the material loss Q_{mat} is defined to be

$$Q_{mat} = 2\pi \frac{P_0 dt}{P_0 \alpha x dt} = 2\pi \frac{P_0 dt}{P_0 \alpha \frac{\lambda}{n} dt} = \frac{2\pi n}{\lambda \alpha}, \tag{2.25}$$

where λ is the resonant wavelength, n represents the refractive index of cavity medium for the given wavelength. The power loss detected at 630 nm wavelength with the optical attenuation is about 7 dB/km, which equals 1.612 per km for silica[2]. So, we can evaluate the intrinsic Q_{mat} for a silica cavity in air to be about 5.679×10^9 at 630 nm wavelength. However, when the cavity is immersed in a solution for in-vivo biodetection [1,39], the material loss is dominated from the liquid. Then, the material loss should be $Q_{mat} \simeq Q_{water} = \frac{2\pi n_{water}}{\lambda \alpha_{water}}$. It is known that the refractive index of water at 630 nm wavelength is about $\widetilde{n} = n + i\kappa = 1.332 + 2.23 \times 10^{-8} i$ [40]. According to the Lambert formula $\alpha(\lambda) = 4\pi\kappa(\lambda)/\lambda$ [41], we can calculate the attenuation coefficient of water at 630 nm, $\alpha_{water} = 450$ per km. Thus, the material loss of microcavity in aqueous environment is worked out to be $Q_{mat} = 2.95 \times 10^7$. This is the estimated value for the material loss under the assumption that all of the light is traveling in the water which is not the case since most of the light is confined in silica. Consequently, the Q_{mat} should be somewhere between 5 billion and 30 million which depends on the mode profile. Therefore, in order to get a more accurate Q_{mat} for a specialized microcavity, numerical simulation is necessary.

One method to evaluate the Q_{mat} is to calculate the effective attenuation coefficient α_{eff} and refractive index n_{eff}. Then substituting them into the Eq. (2.25) to get the Q_{mat} [3]. We work out the Q_{mat}s for a set of toroidal cavities at 630 nm in Fig. 2.5, which have a good agreement with our expectation. As the radius increasing, the material absorption loss becomes smaller which means that less of the light gets out of the toroid structure with a larger major or minor radius. Since the attenuation coefficient of silica is much smaller than water. When the cavity is in an aqueous environment, the material loss is mainly came from the contribution of the water and the Q_{mat} will become larger with increasing radius.

[2] According to the power adsorption formula Eq. (2.24) and the power attenuation formula Attenuation (dB) $=$ $10 \times \log_{10}$(Input Power (W)/ Output Power (W)), $\alpha = 0.1 \times (\ln(P_0/P)/\log_{10}(P_0/P)) \times$ Attenuation $= 0.1 \times \ln(10) \times$ Attenuation $\simeq 0.2303 \times$ Attenuation.

[3] See Appendix.

2.3.2 Radiative Loss

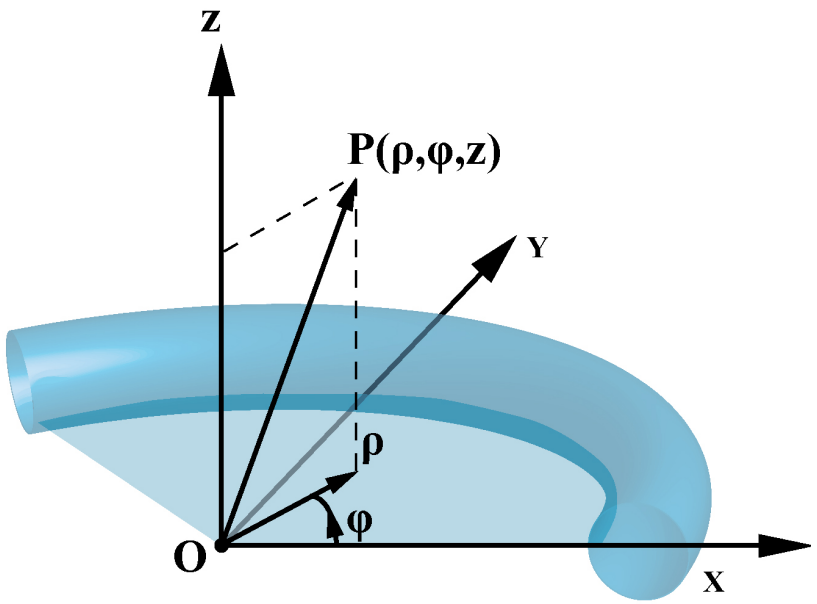

Figure 2.6: Illustration of the cylindrical coordinates for a toroidal microcavity. The origin is at the center of the equatorial plane, and the light is propagating along the azimuthal direction.

In a WGM cavity, most of the confined light circulates around the cavity equator. Considering this rotational symmetry, people use the cylindrical coordinate system ($\widehat{\rho}$, $\widehat{\phi}$,$\widehat{z}$) to describe EM field distribution instead of the Cartesian coordinates ($\widehat{x}$, $\widehat{y}$, $\widehat{z}$) for convenience. In cylindrical coordinates as shown in Fig. 2.6, the unit vectors conversion relations respecting to the Cartesian coordinates are

$$\widehat{\rho} = \widehat{x}\cos(\phi) + \widehat{y}\sin(\phi), \tag{2.26}$$

$$\widehat{\phi} = -\widehat{x}\sin(\phi) + \widehat{y}\cos(\phi), \tag{2.27}$$

$$\widehat{z} = \widehat{z}, \tag{2.28}$$

where $\rho \in [0, \infty)$ is the radial coordinate, $\phi \in [0, 2\pi)$ is the azimuthal coordinate and $z \in (-\infty, +\infty)$ is the the axis coordinate. Then we rewrite the Laplace operator in cylindrical coordinates as below [9]

$$\nabla^2 = \frac{1}{\rho}\frac{\partial}{\partial\rho}(\rho\frac{\partial}{\partial\rho}) + \frac{1}{\rho^2}\frac{\partial^2}{\partial\phi^2} + \frac{\partial^2}{\partial z^2}. \tag{2.29}$$

Substituting the new expression of magnetic field $\mathbf{H} = H^\rho\widehat{\rho} + H^\phi\widehat{\phi} + H^z\widehat{z}$ and new Laplace operator form back into the Helmhöltz equations (2.18). According to the unit vectors relation[4], we obtain

$$\nabla^2 H^\rho - \frac{1}{\rho^2}H^\rho - \frac{2}{\rho^2}\frac{\partial H^\phi}{\partial\phi} + k^2 H^\rho = 0; \tag{2.30}$$

$$\nabla^2 H^\phi - \frac{1}{\rho^2}H^\phi + \frac{2}{\rho^2}\frac{\partial H^\rho}{\partial\phi} + k^2 H^\phi = 0; \tag{2.31}$$

$$\nabla^2 H^z + k^2 H^z = 0, \tag{2.32}$$

and unfold the operator in more details

$$\frac{1}{\rho}\frac{\partial}{\partial\rho}(\rho\frac{\partial}{\partial\rho})H^\rho + \frac{1}{\rho^2}\frac{\partial^2}{\partial\phi^2}H^\rho + \frac{\partial^2}{\partial z^2}H^\rho - \frac{1}{\rho^2}H^\rho - \frac{2}{\rho^2}\frac{\partial H^\phi}{\partial\phi} + \tilde{n}^2 k_0^2 H^\rho = 0; \tag{2.33}$$

$$\frac{1}{\rho}\frac{\partial}{\partial\rho}(\rho\frac{\partial}{\partial\rho})H^\phi + \frac{1}{\rho^2}\frac{\partial^2}{\partial\phi^2}H^\phi + \frac{\partial^2}{\partial z^2}H^\phi - \frac{1}{\rho^2}H^\phi + \frac{2}{\rho^2}\frac{\partial H^\rho}{\partial\phi} + \tilde{n}^2 k_0^2 H^\phi = 0; \tag{2.34}$$

$$\frac{1}{\rho}\frac{\partial}{\partial\rho}(\rho\frac{\partial}{\partial\rho})H^z + \frac{1}{\rho^2}\frac{\partial^2}{\partial\phi^2}H^z + \frac{\partial^2}{\partial z^2}H^z + \tilde{n}^2 k_0^2 H^z = 0, \tag{2.35}$$

where the refractive index $\tilde{n}$ is independent on the ϕ component. After some rearrangements to Eq. (2.35), we arrive at

$$\rho\frac{\partial}{\partial\rho}(\rho\frac{\partial}{\partial\rho})H^z + \rho^2\frac{\partial^2}{\partial z^2}H^z + \rho^2\tilde{n}^2 k_0^2 H^z = -\frac{\partial^2}{\partial\phi^2}H^z. \tag{2.36}$$

Similar as the previous treatment, here we use the variable separation method again and let $H^z = H^z(\rho, z)\Phi(\phi)$, as we are dealing with an axial symmetric system. This yields

$$\Phi(\phi)\rho\frac{\partial}{\partial\rho}(\rho\frac{\partial}{\partial\rho})H^z(\rho,z) + \Phi(\phi)\rho^2\frac{\partial^2}{\partial z^2}H^z(\rho,z) + \Phi(\phi)\rho^2\tilde{n}^2 k_0^2 H^z(\rho,z) = -H^z(\rho,z)\frac{\partial^2}{\partial\phi^2}\Phi(\phi). \tag{2.37}$$

Notice that this has the similar form as the Eq. (2.14), so both sides are divided by

[4] $\frac{\partial\widehat{\rho}}{\partial\rho} = \frac{\partial\widehat{\phi}}{\partial\rho} = \frac{\partial\widehat{z}}{\partial\rho} = 0$; $\frac{\partial\widehat{\rho}}{\partial\phi} = \widehat{\phi}$, $\frac{\partial\widehat{\phi}}{\partial\phi} = -\widehat{\rho}$, $\frac{\partial\widehat{z}}{\partial\phi} = 0$; $\frac{\partial\widehat{\rho}}{\partial z} = \frac{\partial\widehat{\phi}}{\partial z} = \frac{\partial\widehat{z}}{\partial z} = 0$.

$H^z(\rho,z)\Phi(\phi)$ and they must equal to a constant for the same reason. We obtain

$$\frac{1}{H^z(\rho,z)}\rho\frac{\partial}{\partial\rho}(\rho\frac{\partial}{\partial\rho})H^z(\rho,z)+\frac{1}{H^z(\rho,z)}\rho^2\frac{\partial^2}{\partial z^2}H^z(\rho,z)+\rho^2\tilde{n}^2k_0^2=-\frac{1}{\Phi(\phi)}\frac{\partial^2}{\partial\phi^2}\Phi(\phi)=m^2, \tag{2.38}$$

therefore

$$\Phi(\phi)=e^{im\phi}. \tag{2.39}$$

Here m is a complex number, whose real part is the azimuthal mode number of the resonator and imaginary part represents the loss, since $\tilde{n}$ is a complex number, otherwise

$$\begin{aligned}\rho^2\tilde{n}^2k_0^2 &= \rho^2(n+i\kappa)^2k_0^2 \\ &= (n^2-\kappa^2)\rho^2k_0^2+i2n\kappa\rho^2k_0^2,\end{aligned} \tag{2.40}$$

which leads to the unacceptable result that $H^z(\rho,z)=0$, as the imaginary party in the left side of Eq. (2.38) has to equal to zero. Besides, the real part of m is an integer which is the azimuthal order of the whispering gallery mode in a cavity. If we ignore the loss, which is very small compared to the stored energy in a WGM cavity, the EM field must repeat itself in a whispering gallery resonator after each complete round trip. To satisfy this single value condition, we draw the conclusion that $\Phi(2\pi)=1$ which imposes restrictions on m values.

One more consideration here is that the $\frac{\partial}{\partial\phi}$ term in Eq. (2.33) and (2.34) are the radiation terms. They represent loss of energy due to the radiative light along the azimuthal direction during the circulating within the cavity. The radiative loss of a WGM cavity is more complicated than the material loss, which does not have an analytic solution. One direct way to calculate the radiative loss is to integrate the Poynting vector over the whole contour surface which incloses the cavity. This needs to solve the modes of WGM cavity and do it numerically.

2.4 Master Equation

If we ignore the $\frac{\partial}{\partial\phi}$ terms in Eq. (2.33) and (2.34), which are the very small radiation loss parts compared to the rest, the $\Phi(\phi)$ term is separable to all the three magnetic field components H^ρ, H^ϕ and H^z and these three components are decoupled into individual equations (2.33-2.35) in the similar forms. Thus one can rewrite the

expression for magnetic field as below

$$\mathbf{H}(\mathbf{r}) = e^{im\phi}\{H^{\rho}(\rho,z),\ H^{\phi}(\rho,z),\ H^{z}(\rho,z)\}. \tag{2.41}$$

Substituting this expression back into the Maxwell's equations, one obtains

$$\nabla \times \mathbf{H} = [\frac{1}{\rho}\frac{\partial H^{z}}{\partial \phi} - \frac{\partial H^{\phi}}{\partial z}]\widehat{\rho} + [\frac{\partial H^{\rho}}{\partial z} - \frac{\partial H^{z}}{\partial \rho}]\widehat{\phi} + \frac{1}{\rho}[\frac{\partial(\rho H^{\phi})}{\partial \rho} - \frac{\partial H^{\rho}}{\partial \phi}]\widehat{z}, \tag{2.42}$$

and the one set of relations between the six components of the EM field

$$\frac{im}{\rho}H^{z} - \frac{\partial H^{\phi}}{\partial z} = i\epsilon\omega E^{\rho}; \tag{2.43}$$

$$\frac{\partial H^{\rho}}{\partial z} - \frac{\partial H^{z}}{\partial \rho} = i\epsilon\omega E^{\phi}; \tag{2.44}$$

$$\frac{1}{\rho}[\frac{\partial(\rho H^{\phi})}{\partial \rho} - imH^{\rho}] = i\epsilon\omega E^{z}. \tag{2.45}$$

Based on the symmetrical characteristic of EM field, the **E** field is also able to separate the $\Phi(\phi)$ term as **H** field and leads to another set of relations as below

$$\frac{im}{\rho}E^{z} - \frac{\partial E^{\phi}}{\partial z} = -i\mu\omega H^{\rho}; \tag{2.46}$$

$$\frac{\partial E^{\rho}}{\partial z} - \frac{\partial E^{z}}{\partial \rho} = -i\mu\omega H^{\phi}; \tag{2.47}$$

$$\frac{1}{\rho}[\frac{\partial(\rho E^{\phi})}{\partial \rho} - imE^{\rho}] = -i\mu\omega H^{z}. \tag{2.48}$$

By combining these two sets equations for the six components, we finally have the

full set of master equations to describe the EM field behaviors in a WGM cavity

$$\begin{pmatrix} E^{\rho} \\ E^{z} \\ H^{\rho} \\ H^{z} \end{pmatrix} = \frac{i}{q}\Lambda \begin{pmatrix} E^{\phi} \\ H^{\phi} \end{pmatrix}, \tag{2.49}$$

where $q = \mu\epsilon\omega^2\rho^2 - m^2 = k^2\rho^2 - m^2$ and

$$\Lambda = \begin{pmatrix} m\rho(\frac{1}{\rho} + \frac{\partial}{\partial\rho}) & \mu\omega\rho^2\frac{\partial}{\partial z} \\ m\rho\frac{\partial}{\partial z} & -\mu\omega\rho^2(\frac{1}{\rho} + \frac{\partial}{\partial\rho}) \\ -\epsilon\omega\rho^2\frac{\partial}{\partial z} & m\rho(\frac{1}{\rho} + \frac{\partial}{\partial\rho}) \\ \epsilon\omega\rho^2(\frac{1}{\rho} + \frac{\partial}{\partial\rho}) & m\rho\frac{\partial}{\partial z} \end{pmatrix}. \tag{2.50}$$

Thus, from Eq. (2.49) we can see that E^{ρ}, E^{z}, H^{ρ} and H^{z} are represented by the E^{ϕ} and H^{ϕ}. When we put these terms back into the Helmhöltz equations in cylindrical coordinates, there will be two partial differential equations rather than six with only E^{ϕ} and H^{ϕ} terms for us to solve and then the rest four terms of E-field and H-field will be solved automatically. Unfortunately, this partial differential equation is not analytically solvable for the WGM cavities, except the spherical cavity [42]. Even with the numerical simulation, a lot of computational resources are required to solve the electromagnetic problems. However, after taking a closer inspection on the WGM microcavity, one finds that they are all axial symmetric resonators. The problem can be reduced from 3D to 2D depending on this symmetric characteristic, and this will make the numerical calculation much more affordable and efficient [43].

2.5 Mode Volume

The numerical simulation of a WGM cavity resonant field distribution is plotted in Fig. 2.7 through a cross section view. As it illustrated, the circulating light concentrates near the dielectric interface at the equator. A WGM cavity highly confines the EM field in a small physical volume, which is characterized by a parameter called

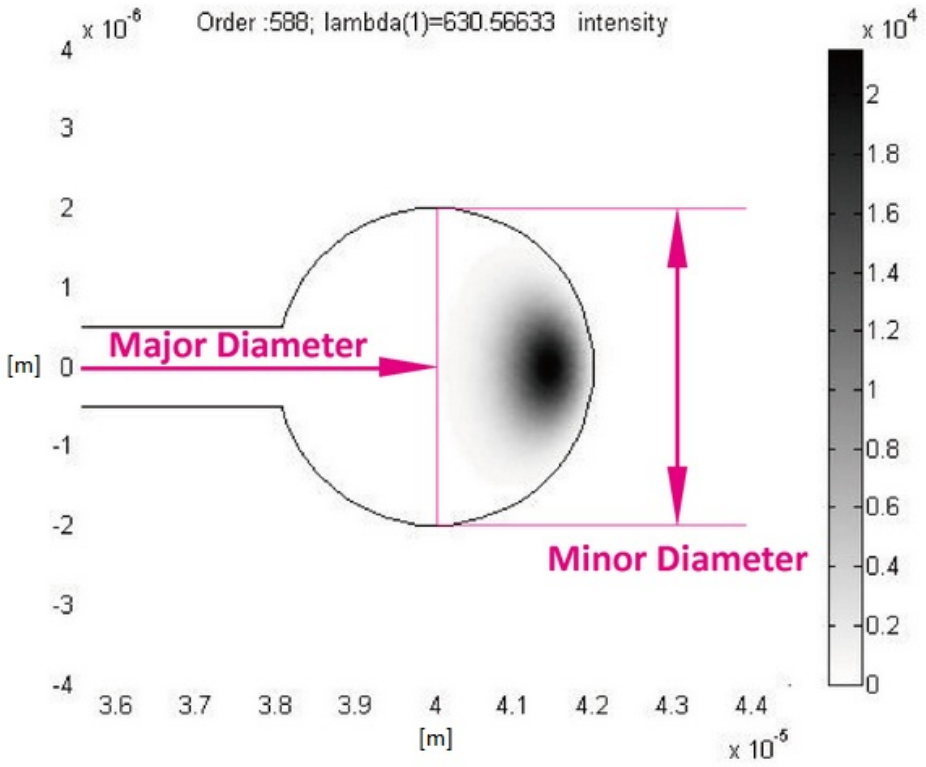

Figure 2.7: The fundamental mode profile of a toroidal WGM microcavity solved by FEM. From the cross section view, the definitions of major and minor diameter of a microtoroid are denoted clearly. We notice that the mode distribution is confined by the dielectric boundary and close to the surface.

mode volume [29], and defined to be[5]

$$V_m = \frac{\int \epsilon_r(\mathbf{r})|\mathbf{E}|^2 dV}{|\mathbf{E}_{max}|^2}. \tag{2.51}$$

An optical microcavity with radius around 40 μm possesses a mode volume about 580 μm^3 as the one shown in Fig. 2.7. Combining with the high circulating power within a WGM cavity, this small mode volume leads to a very high light intensity which enhances the interaction between a photon and an atom significantly. Consequently, physicists believe it is an ideal platform for the quantum electrodynamics investigation [4, 44].

In addition, the mode volume depends on the geometry of a cavity. Microsphere yields larger mode volume as it only confines the light in the radial direction with its

[5]There are several different definitions of mode volume, but they are equivalent in principle.

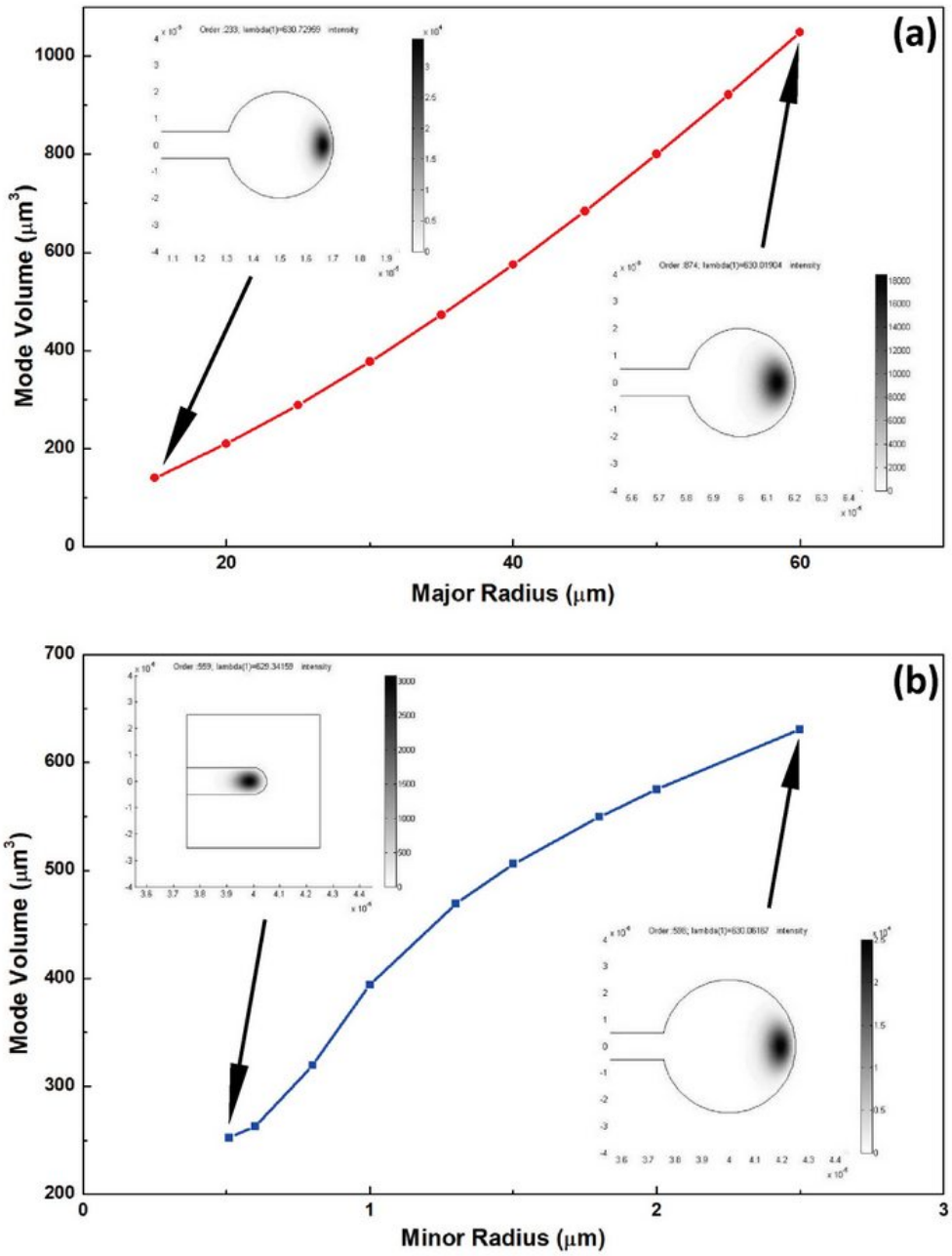

Figure 2.8: The mode volume variation with the size changing of a microtoroid. (a) The minor diameter of a toroid is fixed. The mode volume is proportional to the major radius. Insert: The mode distributions for the toroid with different major diameters. For smaller major diameter, the mode is closer to the interface. (b) The major diameter of a toroid is fixed. The relation between the mode volume and minor diameter is complicated. Notice that the smallest minor diameter equals to the thickness of the silica layer on the pillar which is equivalent to microdisk. Insert: The mode distributions for the toroid with different minor diameters. The mode patterns expand in different directions according to the geometries.

radius varying. Meanwhile, a microtoroid can refine the mode profile with both of its major and minor diameter as shown in the cross section view. The minor radius has limited influence on the mode volume when it is large compared to the resonant wavelength as shown in Fig. 2.8(a). However, its affect becomes considerable when it shrinks in to the size that is comparable to the wavelength. Fig. 2.8(b) illustrates that the slope of mode volume increase is larger for minor radii above 1.5 μm than the ones below. The former is due to the contribution from the change of the total bending radius which has the same effect as that from major radius changes, whereas, the later confines the field distribution along the axial direction to further reduce the mode volume besides the radial direction. Therefore, the microtoroid is advantageous in confining the field distribution and achieving a smaller mode volume comparing to the microsphere. For a WGM based sensor, the mode volume is one of the critical factors that determine the sensitivity. A higher sensitivity requires a smaller mode volume for cavities with the same Q value. As a result, the microtoroid is a better platform as a sensor than the microsphere because of its more efficient mode volume controlling mechanism.

When the light is propagating in an optical waveguide, there is always an evanescently tail out of the boundary. This evanescent field is not a radiative field and is propagating along the waveguide just as the interior part. On the other hand, the reduction of the mode volume increases the evanescent field component out of the cavity (Fig. 2.9). The stronger the evanescent field is, the more sensitive the cavity is to its environment changing. High intensity of the evanescent field is also a perfect exciter for nonlinear optical effects with low threshold power [23, 45].

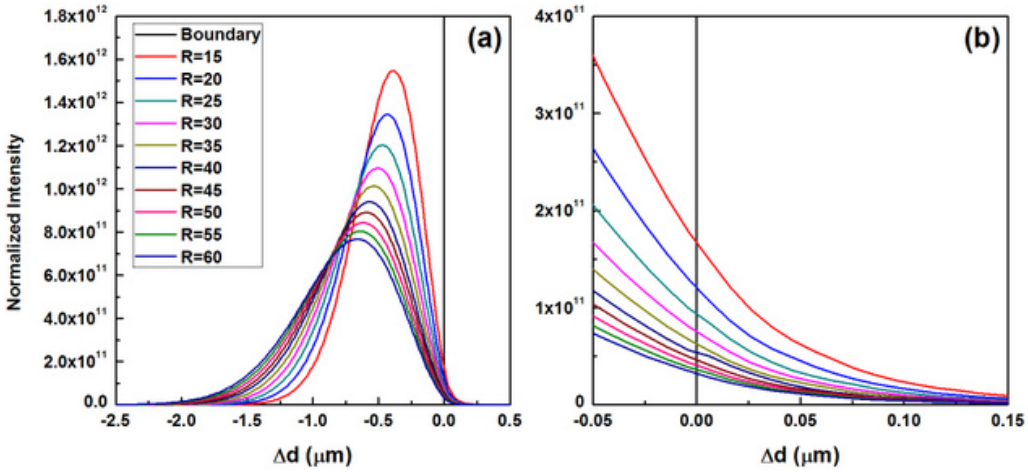

Figure 2.9: The normalized intensity distribution along the radial direction for microtoroids with different major radii (R). (a) Intensity profiles for different radii. The smaller the size is, the higher the maximum intensity is for the same propagating power. (b) The evanescent field of a WGM cavity varying with its mode volume. It decays exponentially and exists for a few hundred nanometers.

Chapter 3

Optical Coupling

One needs to couple the light into a cavity to form the whispering gallery mode. Meanwhile, photons inside the cavity that carry the sensing information need to be coupled out to the measurement apparatus. To excite the WGM and probe the light inside a high Q optical microcavity is another challenge before implementing it for any applications [46]. Since the light is highly confined in a cavity, the direct free space approach is inefficient albeit its simplicity [47]. For some specific applications including cavity QED and nonlinear laser source, the high power circulating in WGM cavity is one of the most desirable properties. Thus, higher coupling efficiency is always important for the coupling techniques between a WGM cavity and the coupler [48, 49].

3.1 Evanescent Field Coupler

Since 1990s, several different kinds of coupling methods have been used to achieve the high efficient coupling. All of these techniques, in principle, are making use of the evanescent field to communicate optical energy between cavity and coupler, as well as the phase information. The phase match condition, that the propagation constants of the WGM at the cavity surface and the mode in coupler need to match each other [50], can ensure the low scattering loss at the coupling junction which is the prerequisite for the low threshold nonlinear optical effects in WGM cavity. The actual Q of the system is restricted by the low coupling quality factor, if the coupling efficiency is reduced due to the phase mismatch [42].

One of the most popular evanescent field couplers is the prism [51, 52]. When a

beam of laser is incident on a prism with higher refractive index than its environment, the total internal reflection (TIR) occurs at the interface at an incidence angle larger than the critical angle, as shown in Fig. 3.1(a). According to the Snell's law, there is no transmitted light across the interface beyond the critical angle. Whilst according to the Maxwell's equations, the boundary conditions of Maxwell's equation require the continuity relation of the EM field components across the dielectric interface [9]. Consequently, the transmitted wave on the other side of the interface does exist in a form of evanescent wave. This wave decays exponentially away from the interface on the order of wavelength. Two optical wave guides can couple light into and out of each other by the evanescent filed when they are placed close enough. By tuning the incident angle of the laser, high efficient coupling with prism is accessible. On the other hand, however, the alignment of a bulk prism is difficult. In addition, this coupling method is difficult to apply to the chip based cavities.

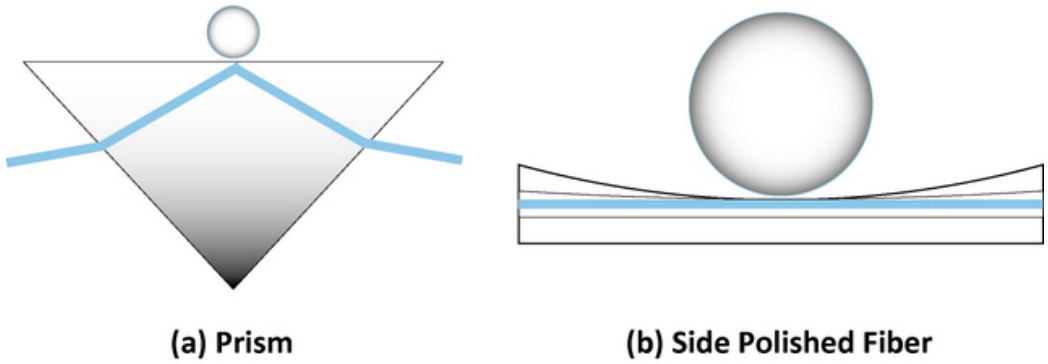

Figure 3.1: Illustration of (a) a prism coupler and (b) a side polished fiber coupler.

Another novel excitation coupler utilizes a side polished fiber [53–55]. This robust coupling method uses an optical fiber as a substrate, shown in Fig. 3.1(b). For a regular fiber, the light is propagating within the fiber core, which is wrapped by cladding and well protected by the polymer jacket [56]. The light is confined due to the continues TIR at the interface between core and cladding. After delicate mechanical polishing, the jacket and cladding of a length of fiber can be polished to sufficient thin (smaller than 0.7 μm). Therefore, the evanescent field in the fiber cladding exposes to the air and is able to couple the light. Because of using a fiber as coupler, the whole optical system can use standard fiber optic components to reduce the alignment difficulty considerably. One problem of the side polished fiber is that

the propagation constant is not tunable, as the structural dimensions of a fiber is fixed. The phase velocity of the light in coupler can not match well with that in a cavity. This will lower the coupling efficiency.

One alternative scheme is to use a fiber taper [49, 50, 57] that can tune the propagation constant through changing the dimension of taper waist to cater for the phase match condition while still maintains all the benefits of the side polished fiber. It can couple the light into a cavity as well as extract light from it [48]. Fig. 3.2 illustrates the tapered fiber coupler in comparison with the original fiber. As shown, the fiber core is vanished when the taper waist becomes thin enough to ensure a sufficient leakage of the evanescent field to the cavity. One may consider it as a cylindrical dielectric waveguide surrounded by air or other medium. This compact coupler can be easily aligned and integrated with any optical cavity and other chip based optical or electrical devices.

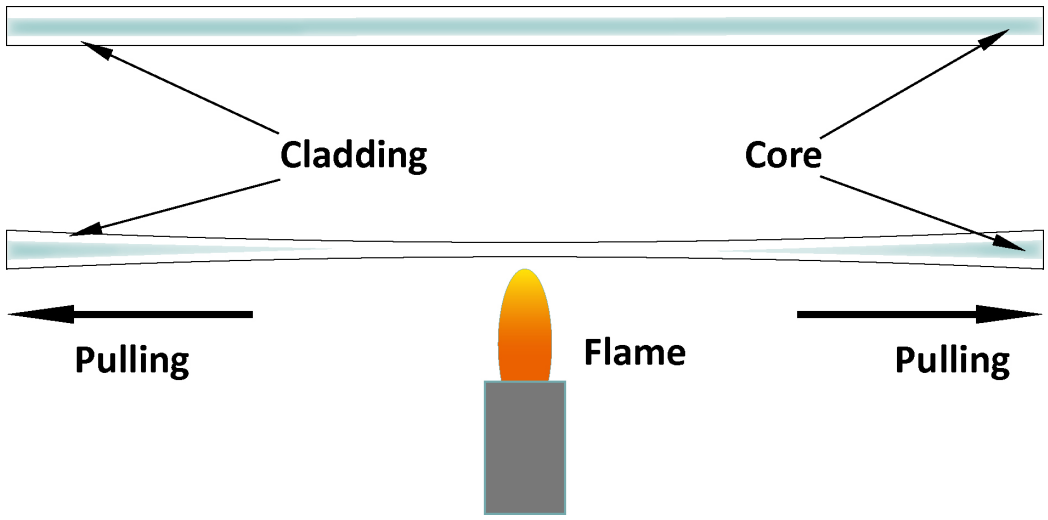

Figure 3.2: The comparison of a fiber taper (below) and a regular fiber (above). The fiber is heated by a torch flame and pulling to the opposite directions until the desired dimension. The fiber core vanishes at the center section of the taper.

3.2 Taper Fabrication

In our lab, we fabricate the optical taper with a standard SM600 single mode fiber for our 630 nm tunable laser source. Fig. 3.3 shows the critical part of our pulling setup on an optical table. One section of the fiber, after proper treatments including stripping off the jacket and cleaning the cladding with IPA, is fixed on the holder

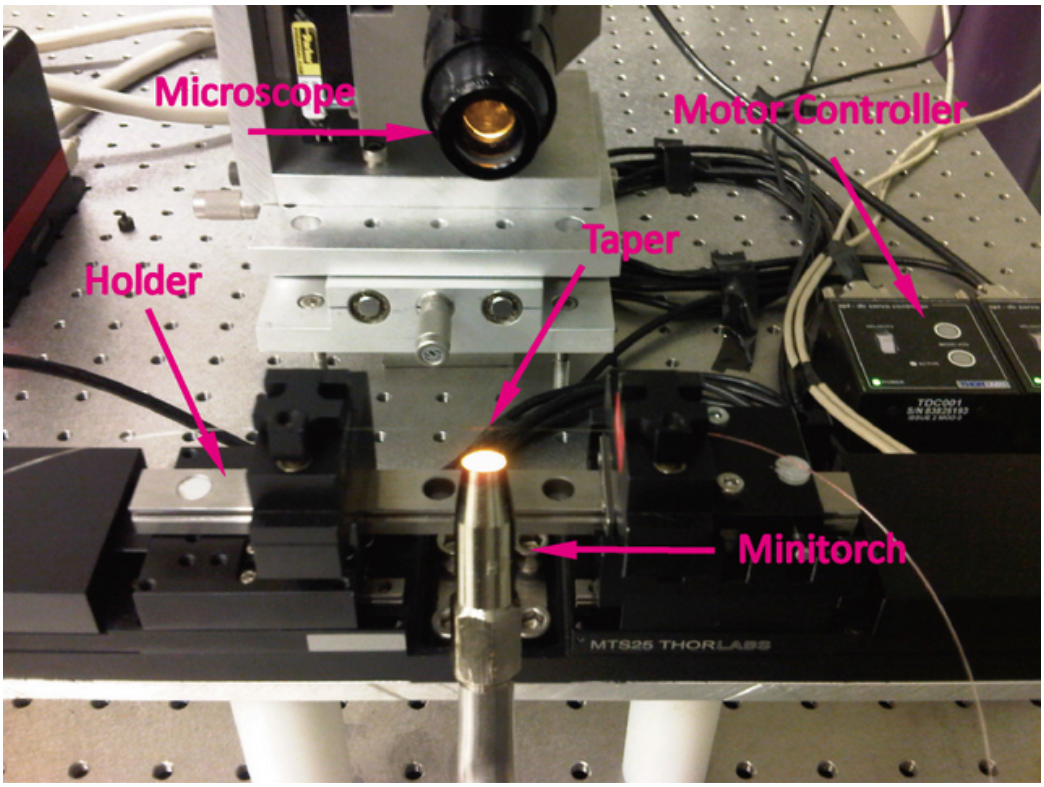

Figure 3.3: The taper pulling setup. The two motor controllers are connected with computers. The pulling process is controlled with a labview programme.

by two magnetic clamps. The holder is sitting on two motorized stages controlled by a home-made software. A hydrogen flame torch is carefully aligned underneath the pulling area, as the quality of final usable taper is highly sensitive to the flame temperature. Once the pulling starts, the center point of the fiber is softened due to the heat and the two clamps moves into the opposite directions synchronously along the trail on the holder. The center section gets thinner as the pulling continues. An oscilloscope is connected to the photodetector to monitor the optical transmission output from the fiber taper while it is pulling. After pulling, the position of the clamps must be fixed by screws. Then, the whole portable holder is ready for moving into the measurement setup.

We can estimate the waist dimension by the normalized frequency V number which is defined by [56]

$$V = \frac{2\pi a}{\lambda} NA = \frac{2\pi a}{\lambda} \sqrt{n_{core}^2 - n_{cladding}^2}, \tag{3.1}$$

where λ is the propagating wavelength in free space which is 630 nm in our case, a is the radius of the taper, n_{core} and $n_{cladding}$ are the refractive indices of the waveguide and its surroundings respectively here. The fiber taper is made of silica which has a refractive index of 1.4457, while $n_{cladding} = 1$ for air. For a single mode waveguide, the V number should be smaller than 2.405 [58]. Therefore, the radius of the taper waist should be smaller than 0.25 μm and 0.43 μm for the air and aqueous environment respectively, when the inside propagating light is single mode. So the taper is fragile if the pulling system is not well optimized.

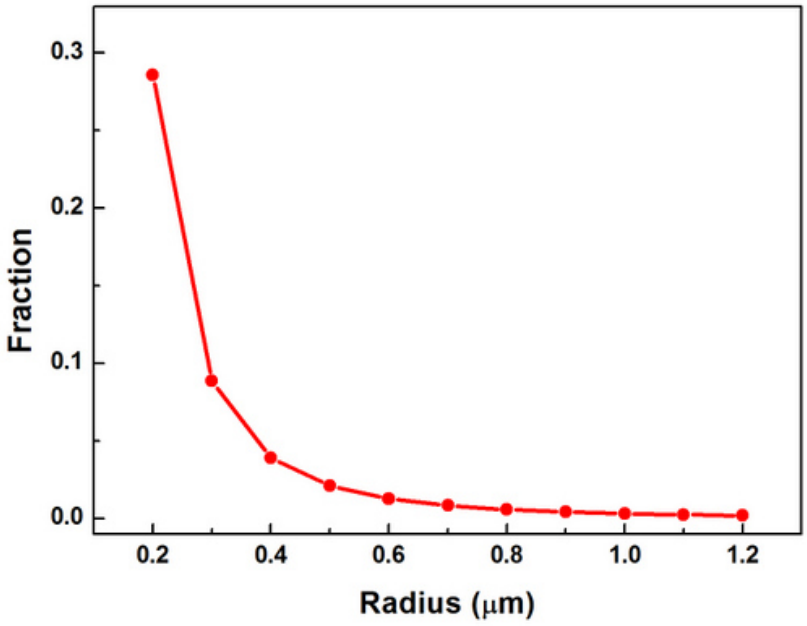

Figure 3.4: The fraction of propagating power out of a taper. It increases fast when the taper waist is small enough.

As the radius of taper waist is getting smaller, more power of the propagating light is distributing out of the taper shown in Fig. 3.4. This means the evanescent field at taper waist is stronger and more efficient to couple the light into a cavity. On the other hand, the refractive indices of silica and air are different, resulting the change of the effective refractive index of the waveguide. This effect is negligible when the radius of a waveguide is relative large and the difference of the refractive indices is small. The effective refractive index is defined as $n_{eff} = \beta/k_0$, where β is the propagating constant and k_0 is the wave number in free space. Because of

the strong evanescent field of the thin taper, the light will experience considerable index changing when traveling through the waist as shown in Fig. 3.5. By slightly modifying the taper waist, the phase match condition between the WGM cavity and the taper can be satisfied and high efficient coupling between them can be achieved.

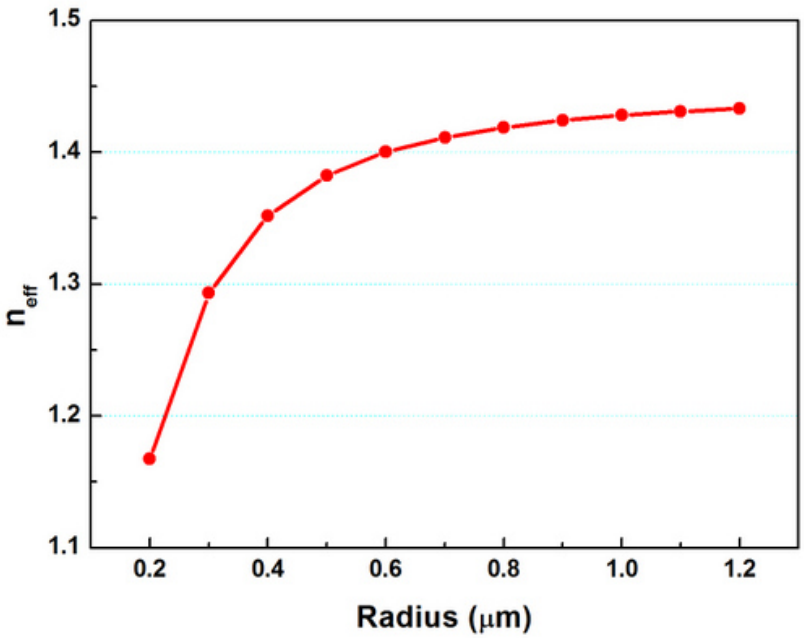

Figure 3.5: The effective refractive index changing with the taper radius. Its value gets close to that of air from silica when the taper size becomes small.

3.3 Mathematical Description

The excitation of the high Q whispering gallery mode from a coupler can be described by a quasi geometrical approximation [59]. There could be multiple modes propagating in both of the cavity and coupler. For simplicity, we assume that both of them are single mode. Thus, the electric field of the fundamental whispering gallery mode in a cavity is $\widehat{E}_w(\rho,\ z)e^{j\omega_0 t}$ at $\phi = 0$. Here, ω_0 is the resonant frequency of the WGM resonator and $\widehat{E}_w(\rho,\ z)$ is normalized such that its power is 1 Watt, as

$$\widehat{P} = \int \frac{c}{n}\epsilon_0\epsilon_r \widehat{E}_w^* \widehat{E}_w ds = c\epsilon_0 \int n(\rho,\ z)\widehat{E}_w^* \widehat{E}_w ds = 1 \text{ Watt}. \tag{3.2}$$

The same to the coupler, our fiber taper, the fundamental mode is $\widehat{E}_f(\rho,\ z)e^{j\omega_0 t}$ at $\phi = 0$, and again it is normalized to

$$\widehat{P} = c\epsilon_0 \int n\widehat{E}_f^* \widehat{E}_f ds = 1 \text{ Watt.} \tag{3.3}$$

Now, we consider that E_f transmits through the taper with laser frequency ω, which is

$$E_f = b_0(t)\widehat{E}_f(\rho,\ z)e^{j\omega t} = b_0(t)e^{j\delta\omega t}\widehat{E}_f(\rho,\ z)e^{j\omega_0 t} = b(t)\widehat{E}_f(\rho,\ z)e^{j\omega_0 t}, \tag{3.4}$$

where $b(t)$ is the amplitude of electric field in taper. So that, we obtain the propagating power in the taper is

$$P_f = c\epsilon_0 \int nE_f^* E_f ds = |b_0|^2 \widehat{P} = |b_0|^2 \text{ Watt.} \tag{3.5}$$

We further assume that the coupling coefficient T and reflection coefficient R hold the relation $|T|^2 + |R|^2 = 1$ by neglecting the reflection loss at the coupling junction. Due to the total internal reflection at the silica air interface, the fraction of light coupled from taper to cavity is small, typically close to one percent. Therefore, most of light still travels along the taper, and the reflection coefficient can be expressed as $R = \sqrt{1 - T^2} \simeq 1 - T^2/2 \sim 1$. One more consideration needs to be made is that the taper coupling to cavity is approximate the same as cavity to taper at the junction due to symmetry of the system as shown in Fig 3.6. Therefore, the electric field in cavity at $t > 0$ is

$$\begin{aligned} E_w &= a_0(t)\widehat{E}_w(\rho,\ z)e^{j\omega t} \\ &= a_0(t)e^{j\delta\omega t}\widehat{E}_w(\rho,\ z)e^{j\omega_0 t} \\ &= a(t)\widehat{E}_w(\rho,\ z)e^{j\omega_0 t}, \end{aligned} \tag{3.6}$$

where $a(t)$ is the amplitude of the electric field in the cavity.

Based on all the above descriptions, one can work out the equation for the propagating mode in the resonator at the beginning of the next round trip. It is a superposition of the coupled field from the taper and the reflected field from the last round. This yields [59]

$$a(t) = jTb(t) + Ra(t - \tau_c)e^{j\frac{2\pi n_e L}{\lambda} - \frac{\alpha_0 L}{2}}, \tag{3.7}$$

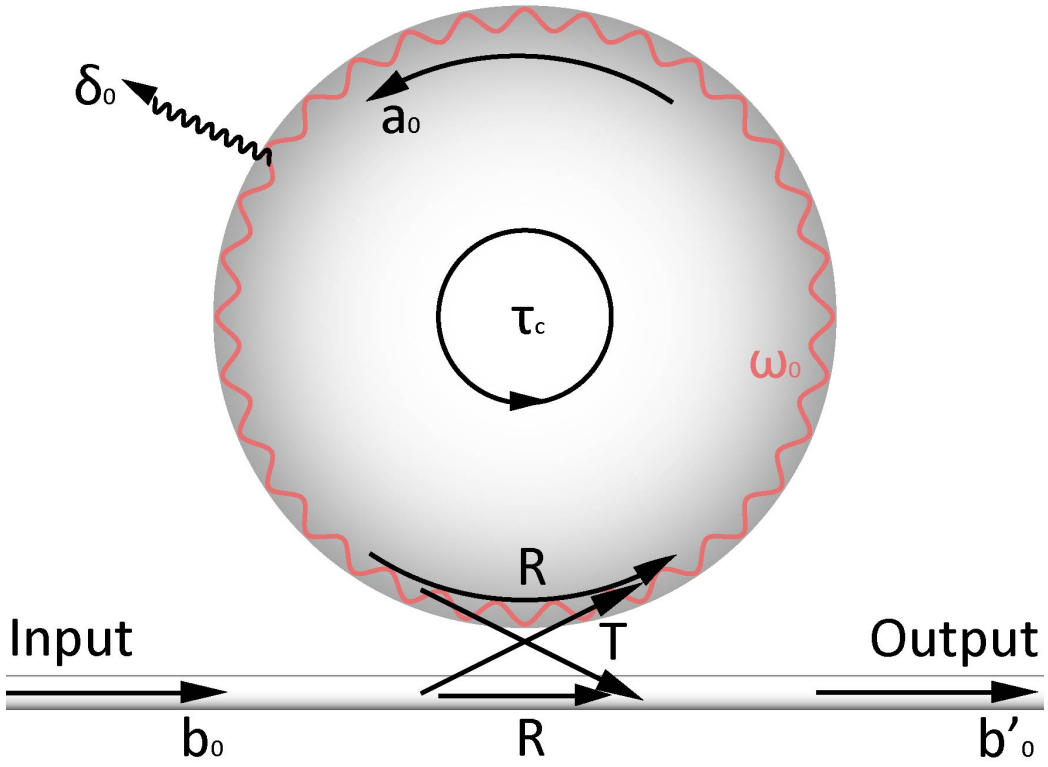

Figure 3.6: An illustration of the coupling between a cavity and a taper. b_0 and b_0' are the input and output of the taper. a_0 is the WGM in cavity. δ_0 represents the cavity loss. The light in both of the cavity and taper couple into each other according to the coefficient T. The total transmission is a superposition of the reflection and the coupling.

where n_e is the effective refractive index, which can be replaced by the refractive index of silica here, as most light is confined within the cavity; $a(t) = a_0(t)e^{j\delta\omega t}$ is the amplitude of propagating mode in cavity; $b(t) = b_0(t)e^{j\delta\omega t}$ is the amplitude of propagating mode in taper; L is the light path which roughly equals to the circumference $L = 2\pi r$, as the light is propagating very close to the surface of the cavity; $\tau_c = n_e L/c$ is the circulating time for the light traveling one complete round trip; α_0 is the linear attenuation[1], in our case which contains two important components, material loss α_{mat} and radiation loss α_{rad}. An additional point about Eq. (3.7) needs

[1]The linear attenuation α is a coefficient of power loss. Since $P \propto E^2$ and $P = P_0 e^{-\alpha x}$, here we use $\alpha/2$ for the electric field attenuation.

to be discussed is that

$$e^{j\frac{2\pi n_e L}{\lambda}} = e^{j\omega\frac{n_e L}{c}} = e^{j\delta\omega\frac{n_e L}{c}} e^{j\omega_0\frac{n_e L}{c}} = e^{j\delta\omega\frac{n_e L}{c}} e^{j2\pi\frac{n_e L}{\lambda_0}}. \tag{3.8}$$

In the last term, λ_0 is the resonant wavelength. For a whispering gallery resonator, the round optical path must be an integral multiple of the resonate wavelength so that $n_e L/\lambda_0$ is an integer which is the azimuthal mode number, i.e. $e^{j2\pi\frac{n_e L}{\lambda_0}} = e^{j2\pi m} = 1$.

By expanding $a(t-\tau_c)$, we obtain $a(t-\tau_c) = a(t) - \tau_c da(t)/dt$. This yields, with Eq. (3.7),

$$a(t) = jTb(t) + R[a(t) - \tau_c\frac{da(t)}{dt}]e^{j\frac{2\pi n_e L}{\lambda} - \frac{\alpha_0 L}{2}}. \tag{3.9}$$

Meanwhile, taking the full derivative of the cavity mode amplitude $a(t)$ with respect to time, we know that

$$\frac{da(t)}{dt} = \frac{da_0(t)e^{j\delta\omega t}}{dt} = \frac{da_0(t)}{dt}e^{j\delta\omega t} + j\delta\omega a_0(t)e^{j\delta\omega t}. \tag{3.10}$$

The equation for the propagating electric field amplitude in cavity (Eq. (3.7)) can be rewritten as below

$$\begin{aligned} a_0(t)e^{j\delta\omega t} = jTb_0(t)e^{j\delta\omega t} + R[a_0(t)e^{j\delta\omega t} - \tau_c\frac{da_0(t)}{dt}e^{j\delta\omega t} \\ -\tau_c j\delta\omega a_0(t)e^{j\delta\omega t}]e^{j\delta\omega\tau_c - \frac{\alpha_0 L}{2}}. \end{aligned} \tag{3.11}$$

Eliminate the $e^{j\delta\omega t}$ term from both sides of the above equation and rearrange, we get

$$R\tau_c e^{j\frac{2\pi n_e L}{\lambda} - \frac{\alpha_0 L}{2}}\frac{da_0(t)}{dt} + \{1 - R[1 - j\delta\omega\tau_c]e^{j\delta\omega\tau_c - \frac{\alpha_0 L}{2}}\}a_0(t) = jTb_0(t), \tag{3.12}$$

or more clearly in a short form as below

$$\frac{da_0(t)}{dt} + \frac{1}{\tau_c}[\frac{1}{R}e^{-j\delta\omega\tau_c}e^{\frac{\alpha_0 L}{2}} - 1 + j\delta\omega\tau_c]a_0(t) = jCb_0(t). \tag{3.13}$$

Here, we introduce a mode matching parameter $C = \frac{T}{R}e^{-j\delta\omega\tau_c}e^{\frac{\alpha_0 L}{2}}$, which is a representation of the coupling matching between the mode in cavity and taper[2]. With the approximations $1/R \simeq 1 + T^2/2$, $e^{\frac{\alpha_0 L}{2}} \simeq 1 + \alpha_0 L/2$ and $e^{-j\delta\omega\tau_c} \simeq 1$[3], we finally arrive

[2]Basically, the phase velocity of the light in coupler should be close to that in a cavity, and the distance between them should be properly aligned.

[3]Under the condition: $T \ll 1$, $\alpha_0 L/2 \ll 1$ and $\delta\omega\tau_c \ll 1$.

at the coupling condition for the cavity and taper modes

$$\frac{da_0(t)}{dt} + (\delta_c + \delta_0 + j\delta\omega)a_0(t) = jCb_0(t). \tag{3.14}$$

Eq. (3.14) describes the relation between the exciting mode in a taper and the WG mode in a cavity, in which $\delta_c = T^2/(2\tau_c)$ is the coupling loss term and $\delta_0 = \alpha_0 c/(2n_e)$ is the intrinsic loss term, which contains the material loss and radiation loss as we discussed in previous chapter.

To be more explicit, let us further develop the Eq. (3.14). Multiple the complex conjugate of Eq. (3.14) by $a_0(t)$ and the equation itself by $a_0^*(t)$, and take the sum of the two products. The expression becomes

$$a_0(t)\frac{da_0^*(t)}{dt} + a_0^*(t)\frac{da_0(t)}{dt} + a_0^*(t)a_0(t)2Re\{\delta_c + \delta_0\} = 2Re\{jCb_0(t)a_0^*(t)\}. \tag{3.15}$$

Notice that $|a_0(t)|^2 = P_w$ is the circulating power in a cavity and $|b_0(t)|^2 = P_f$ is the propagating power in a taper. This leads to the relation of the optical powers between cavity and taper

$$\frac{dP_w}{dt} + 2\delta P_w = \Gamma P_f, \tag{3.16}$$

where $2\delta = 2\delta_c + 2\delta_0$ is the relative loss rate including contributions from both coupling and intrinsic and $\Gamma = 2Re\{jCa_0^*(t)/b_0^*(t)\}$. If one turns off the input power, i.e. $P_f = 0$, Eq. (3.16) becomes

$$2\delta = -\frac{dP_w}{P_w dt}. \tag{3.17}$$

Taking the definition of quality factor into account

$$Q = 2\pi\frac{P_w}{\tau_0\frac{dP_w}{dt}} = \frac{\omega_0}{2\delta}, \tag{3.18}$$

we get the expression for the total quality factor and its components as it first given in Chapter 2,

$$\frac{1}{Q_{total}} = \frac{2\delta}{\omega_0} = \frac{2\delta_{mat}}{\omega_0} + \frac{2\delta_{rad}}{\omega_0} + \frac{2\delta_c}{\omega_0} = \frac{1}{Q_{mat}} + \frac{1}{Q_{rad}} + \frac{1}{Q_{coupling}}. \tag{3.19}$$

Also, the first term which is the material absorption loss $Q_{mat} = \omega_0/(2\delta_{mat}) = 2\pi n_e/(\alpha_{mat}\lambda_0)$ is consist with what we have shown previously.

3.4 Transmission

Next, considering the stationary condition of Eq. (3.14), i.e. $da_0(t)/dt = 0$, which is also the working condition for the WGM cavity sensing, we have

$$(\delta_c + \delta_0 + j\delta\omega)a_0(t) = jCb_0(t). \tag{3.20}$$

Under this stationary condition, combining with the output electric field amplitude of the taper from the internal reflection and coupling from the cavity

$$b_0'(t) = jTa_0(t) + Rb_0(t), \tag{3.21}$$

we provide the expression of the output transmission from the taper as below

$$b_0'(t) = b_0(t)\left(1 - \frac{2\delta_c}{\delta_c + \delta_0 + j\delta\omega}e^{-j\delta\omega\tau_c + \frac{\alpha_0 L}{2}}\right). \tag{3.22}$$

Here, we assume $R \simeq 1$ as the coupled evanescent field is much smaller than the propagating field. Besides, the high Q of our cavity guarantees that the loss energy is so small compared to the stored energy that we can safely assume $e^{\frac{\alpha_0 L}{2}} \simeq 1$ here. Thus, the output power of the taper is a function of input power $|b_0(t)|^2$ and the frequency shift $\delta\omega$

$$|b_0'(t)|^2 = |b_0(t)|^2[1 - \frac{4\delta_c\delta_0}{(\delta_c + \delta_0)^2 + \delta\omega^2}]. \tag{3.23}$$

So the normalized transmission is defined to be

$$\begin{aligned}
\frac{|b_0'(t)|^2}{|b_0(t)|^2} &= 1 - \frac{4\frac{\omega_0}{2Q_c}\frac{\omega_0}{2Q_0}}{(\frac{\omega_0}{2Q_c} + \frac{\omega_0}{2Q_0})^2 + \delta\omega^2} \\
&= 1 - \frac{4Q_cQ_0}{(Q_c + Q_0)^2 + (2Q_cQ_0\frac{\delta\omega}{\omega_0})^2} \\
&= 1 - \frac{4K}{(1+K)^2 + (2Q_0\frac{\delta\omega}{\omega_0})^2},
\end{aligned} \tag{3.24}$$

where $K = Q_0/Q_c$ is the normalized coupling parameter.

This normalized transmission should have a value between 0, which means no output, and 1, that little light is coupled into the cavity. Additionally, when the WGM cavity is in resonant condition, the light frequency equals to the resonant

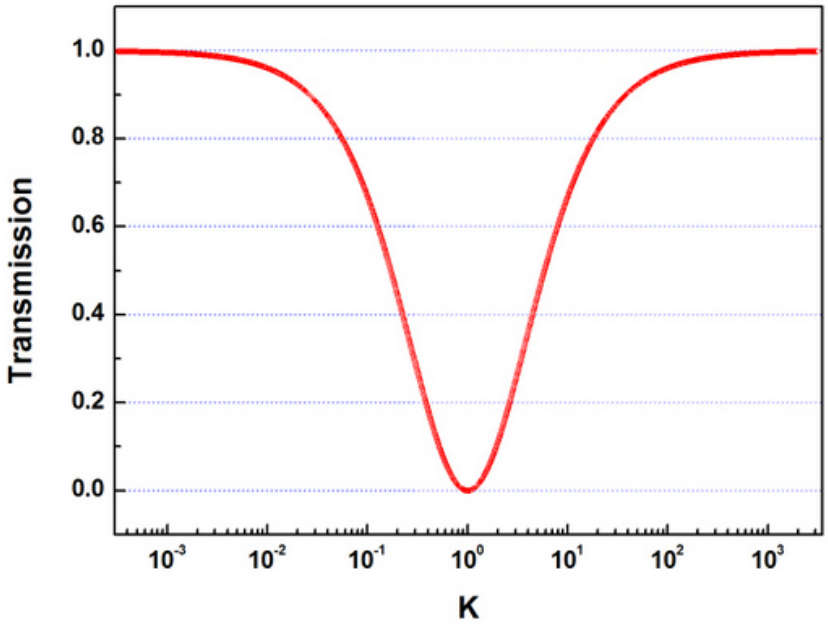

Figure 3.7: The normalized transmission of the taper vs the normalized coupling parameter K. When $K = 1$ which means the coupling loss equals to the cavity intrinsic loss, the transmission drops to zero. This point is called critical coupling.

frequency ω_0, which means the frequency shift $\delta\omega = 0$. Eq. (3.24) reduces to

$$\frac{|b_0'|^2}{|b_0(t)|^2} = 1 - \frac{4K}{(K+1)^2}. \tag{3.25}$$

This equation states that the normalized transmission is a function only depends on the coupling parameter K under the resonant condition. The relation between the transmission and coupling is plotted in Fig. 3.7 according to Eq. (3.25). As it demonstrated that the transmission spectrum can de divided into three regions $K = 1$ where the transmission is zero, $K < 1$ and $K > 1$ where the transmission recovers when K is getting away from the unit.

3.4.1 Under Coupling

When the coupling parameter is smaller than one, the system is in the undercoupling region. In this region, the coupling loss is smaller than the intrinsic loss of the cavity, since $Q_0 < Q_c$. If the taper is far away from the cavity, there is no light coupled into

the cavity or the coupling loss. When the taper gets closer to the cavity gradually, one small part of light couples into the cavity from the evanescent field of the taper. However, the coupling is so weak that the coupled energy is just as much as or slightly larger than the cavity loss. This small amount of pumping light accumulates in the cavity, and couples back to the taper. As a result, it interferes destructively with the light in taper and causes the decrease of the transmission. The closer to the cavity the taper gets, the lower the transmission becomes until to zero.

3.4.2 Over Coupling

In over coupling region, on the other hand, the coupling is strong. The majority of the light in the taper is coupled into the cavity, meanwhile as a symmetrical mechanism, more light will coupled back to the taper. The coupling loss becomes the dominant loss mechanism of the cavity beyond the intrinsic loss. Considering the accumulated circulating power in cavity is several orders higher than that in taper. The coupled back light is far stronger than the remained light in the taper even it is only a small fraction of the circulating light confined in a cavity. It maintains the high transmission in the taper. One can move the taper away from the cavity to reduce the coupling and lower the transmission.

3.4.3 Critical Coupling

At the $K = 1$ point, it is the critical coupling, at which the coupling loss equals the intrinsic loss. Since the transmission is zero, all of the input power is coupled into the cavity. The cavity accumulates its highest power. It requires the taper has a strong evanescent field and the phase velocity of the traveling light is close to that in cavity. Then, during the measurement experiments, one can always achieve the critical coupling through adjusting the distance between taper and cavity.

3.5 Measuring Q by Bandwidth

When a taper is coupled with a cavity, there is a Lorentzian dip at the resonant location on the transmission by scanning the wavelength within a small range (Fig. 3.8). The bottom point of the transmission dip is at the resonant frequency $\omega = \omega_0$ with a frequency mistuning $\delta\omega = 0$. From the half depth of the transmission dip, derived in

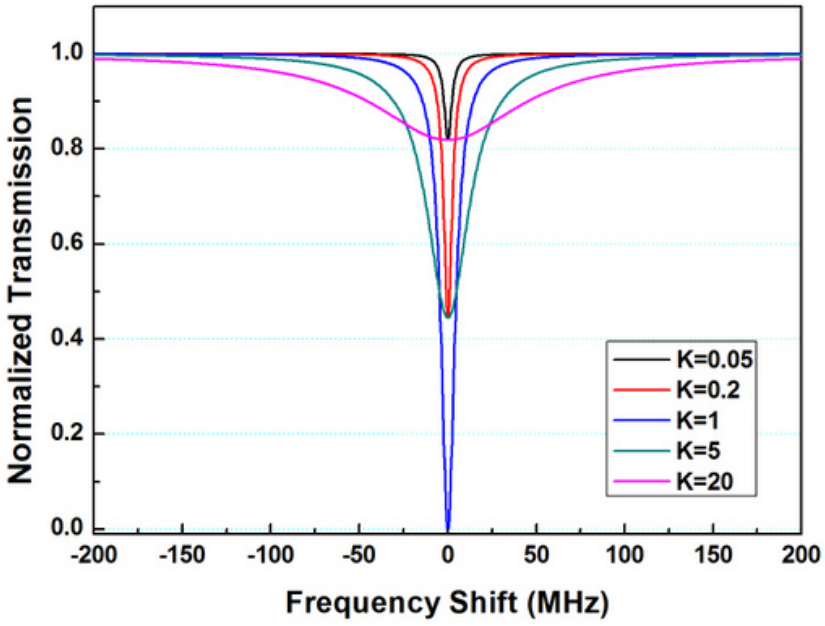

Figure 3.8: The normalized transmission spectrum of different coupling conditions as scanning the frequency of the light. The output transmission becomes zero at resonant frequency only under the critical coupling condition. When the normalized coupling parameter gets away from the unit, the transmission dips are weaker. The dips become narrower in the under coupling region, while in the over coupling region, the dips broaden.

Eq. (3.24), one can obtain

$$Q_c + Q_0 = 2Q_cQ_0\frac{\delta\omega}{\omega_0}. \tag{3.26}$$

This yields another expression for the quality factor, combing with the relation of the total quality factor and its components, $Q_{total} = Q_0Q_c/(Q_0 + Q_c) = \omega_0/(2\delta\omega)$. Notice that $\Delta\omega = 2\delta\omega$ is the full width at half maximum (FWHM) of the Lorentz dip. This expression offers us another way to measure the loaded quality factor besides the ring down measurement. Taking the relation between frequency and wavelength into consideration, we denotes an equivalent definition of the quality factor as

$$Q = \frac{\omega_0}{\Delta\omega} = \frac{\lambda_0}{\Delta\lambda}, \tag{3.27}$$

where ω_0 is the resonant frequency and λ_0 is the resonant wavelength. We use this method to measure the WGM cavity quality factors in all our experiments.

As illustrated in Fig. 3.8 that, for a typical high Q cavity $Q_0 = 10^8$, the FWHM of the Lorentz dip is getting broader with the increasing of K. This indicates that the decrease of the coupling Q reduces the total quality factor. Under the critical coupling condition, the loaded quality factor is expected to reduce to 5×10^7, or half of the intrinsic quality factor. When the coupling becomes weaker, the width of the transmission dip gets narrower and the loaded quality factor becomes very close to the intrinsic quality factor. One can measure the intrinsic quality factor of a cavity by coupling very little light into the cavity in real experiments. This trend is plotted in Fig. 3.9.

Finally, the FWHM is inversely proportional to the quality factor according to Eq. (3.27). For a $Q_0 = 10^8$ cavity, the bandwidth as narrow as 4.8 MHz with a probe laser wavelength of 630 nm is obtainable. The narrower the bandwidth is, the higher accuracy one gets to localize the resonant frequency. As a result of the ultra high spectrum resolution we got from a high Q WGM cavity, a very small resonate frequency shift due to the perturbation on cavity modes from the environment influence becomes detectable. Based on this mechanism, people use it as a high sensitive sensors, so that cavities with higher Q are always preferred.

3.6 Buildup Factor

Under the stationary condition, the coupled light from taper to cavity compensates the loss of the cavity. Eq. (3.20) shows the relation between the electric field amplitude in taper and that in cavity and offers a way for us to estimate the circulating power inside a WGM cavity. Noticing that the input power in taper $P_f = |b_0(t)|^2$ and circulating power in cavity $P_w = |a_0(t)|^2$, we change Eq. (3.20) into

$$\frac{|a_0(t)|^2}{|b_0(t)|^2} = \left| \frac{1}{\delta_c + \delta_0 + j\delta\omega} \frac{jT}{R\tau_c e^{-\frac{\alpha L}{2}}} \right|^2 . \tag{3.28}$$

When the WGM cavity is under the resonant condition, the light frequency equals to the resonant frequency ω_0 that means the frequency mistuning $\delta\omega = 0$. The linear attenuation term $e^{-\frac{\alpha L}{2}}$ can be ignored, because the power loss is extremely small in our cavity, which is several orders smaller than the circulating power. Consequently,

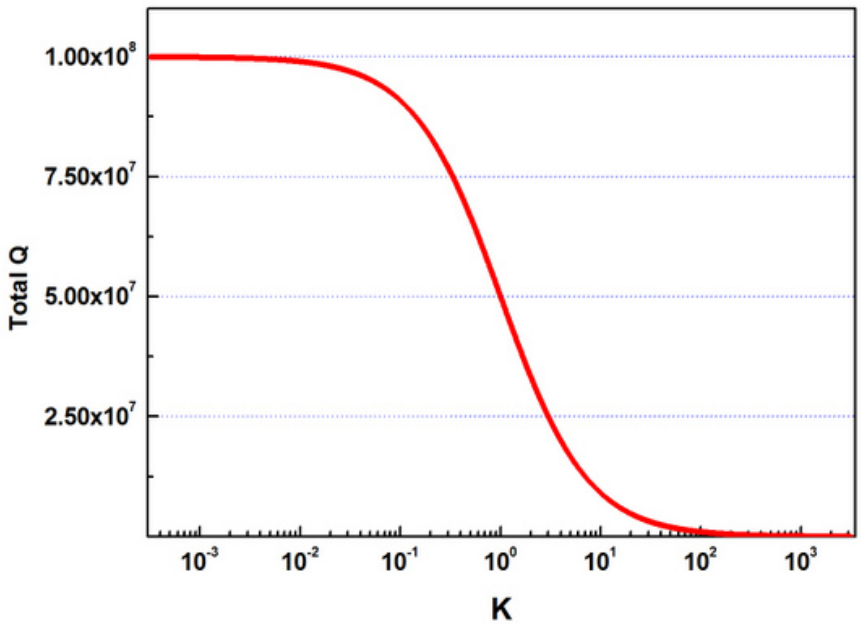

Figure 3.9: The relation between the total quality factor and the normalized coupling parameter for a $Q_0 = 10^8$ cavity. When the coupling is weak enough, the loaded Q measured by linewidth equals to the intrinsic Q.

we introduce the buildup factor (B) to characterize the amplification of the input power by a cavity as

$$\begin{aligned} B &= \frac{1}{(\delta_c + \delta_0)^2} \frac{T^2}{R^2 \tau_c^2} \\ &= \frac{1}{(\frac{\omega_0}{2Q_c} + \frac{\omega_0}{2Q_0})^2} \frac{\omega_0}{Q_c \tau_c} \\ &= \frac{\lambda Q_0}{\pi^2 n_e L r} \frac{K}{(K+1)^2} \end{aligned} \tag{3.29}$$

where K is the normalized coupling parameter.

The buildup factor as a function of the coupling condition is plotted in Fig. 3.10. It clearly shows that the buildup factor reaches the maximum at the critical coupling point. This is consist with that all the light is coupled into the cavity. The power circulating in a cavity can be calculated with the buildup factor. For instance, if an input laser excites the WGM cavity at the critical coupling condition with 1 mW, the circulating power will be higher than 10W. Because of the low loss, the WGM cavity

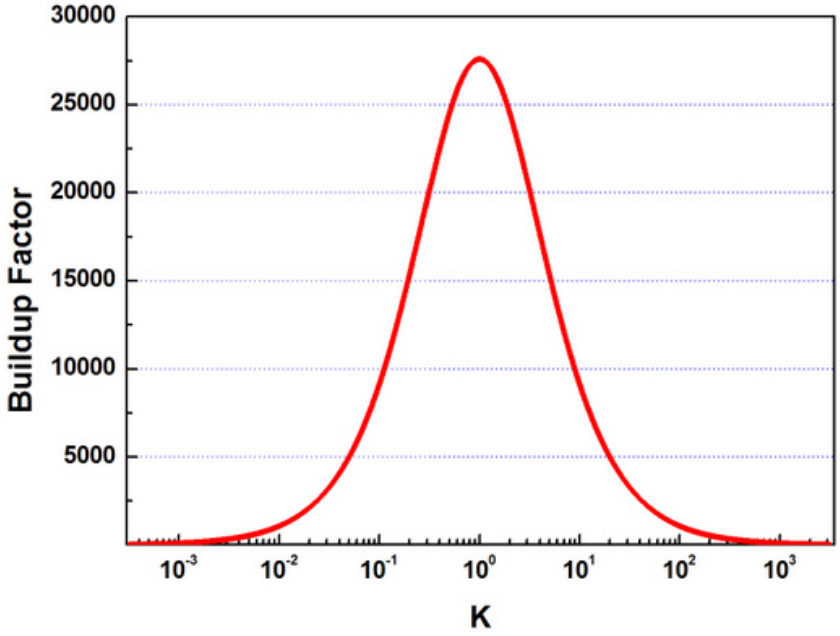

Figure 3.10: The buildup factor plot with normalized coupling parameter K. This states that the circulating power reaches the maximum at the critical coupling point.

can enhance the optical power significantly as well as the evanescent field. Many researchers are interested in using WGM cavities to investigate the nonlinear optical effects, as it has the ability to reduce the threshold power greatly.

In addition, the enhancement of the input power also depends on the intrinsic quality factor of a cavity according to Eq. (3.29). As shown in Fig. 3.11, the circulating power increases with the intrinsic quality factor. This is another reason that we are always pursuing the cavity with higher Q.

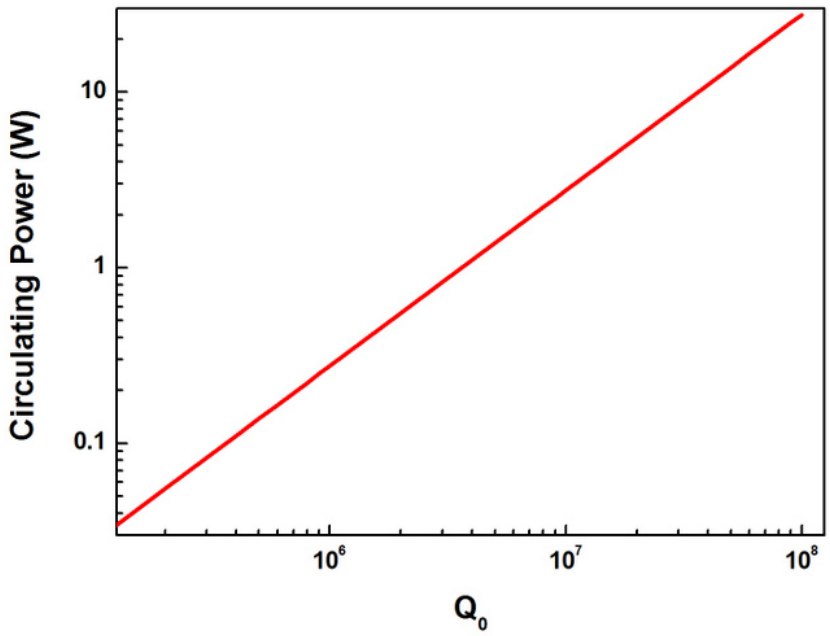

Figure 3.11: The maximum optical power circulating in a WGM cavity is proportional to its intrinsic quality factor for 1 mW input power.

Chapter 4

A Mode Solver Based on Straight Waveguide Modes

The numerical simulation is a powerful tool to direct the experiments. In particular, because of the complex of microtoroid, there is no analytic solver for its mode and the current numerical mode solver is difficult to implement. Up to date, modeling of WGM and estimation of Q in a microcavity are achieved through the first principle numerical techniques such as finite element method (FEM) [43, 60]. Such techniques provide satisfactory accuracy but require sophisticated implementation and provide few physical insights into the wave behavior in the microcavity. On the other hand, bent fiber and waveguide structures have been intensively studied in the 1970s with the boom of fiber optical communication [61, 62]. Although a WGM microcavity can be viewed as the closed-loop of a bent waveguide, little research have been carried out to transfer the analytical techniques for bent waveguides to microcavities.

Here we develop a full vector mode solver for axisymmetric microcavities by expanding the microcavity modes as series of modes from a corresponding straight waveguide. The analysis of the cavity mode and Q can be carried out in analogy to the study of propagation modes and loss of a bent waveguide [63]. For simplicity, here we implement the techniques on a silica microtoroid platform [5]. The implementations on other platforms such as, microspheres, microdisks, etc. can be directly carried out.

The fiber modes for this work are calculated with a commercial software package COMSOL based on the FEM for simplicity while the analytical form of such modes is widely available [56]. The modes of a microtoroid is solved in a more efficient way

using these straight fiber modes. Here, given that such a cavity has a circular cross section and can be viewed as a closed fiber loop in micrometer scale, we implement a novel mode solver by expanding the WGM mode on an orthonormal set of fiber normal modes. Further, using the well-established theory on bent fiber loss [62], we provide an accurate estimation of cavity quality factor. Finally, this technique provides a different angle to interpret the wave propagation behavior in WGMs, making it possible to setup a beam propagation method (BPM) simulation based on this solver.

4.1 Theory

A silica microtoroid is a toroidal shaped optical microcavity [5]. As its cross section is identical to that of an optical fiber, it is nature to be viewed as a closed fiber loop in micron scale. Therefore, analysis of the bent fiber structure [63, 64] can be applied with the exception that a closed loop will introduce resonance when the optical path length coincides with the multiples of wavelengths.

4.1.1 Mode solver based on step index fiber

One Italian group developed a mode solver for bent waveguides in a similar way based on BPM [64]. In our analysis, we apply a cylindrical coordinate system (ρ, ϕ, z') as shown in Fig. 4.1. The origin of the coordinate (o) is at the center of the toroid and the light propagates along the azimuthal direction. In analogy, a fiber is placed in a local cartesian coordinate (x, y, z) with the center of the fiber at the coordinate origin (o'), here the z-direction is the light propagation direction and the x and y direction are corresponding to the radial and axial direction in the cylindrical coordinates respectively. Hence, all the six components of the electromagnetic (EM) field in the toroid can be denoted equally with the cylindrical or cartesian coordinates. For example, the H_ϕ component denoted for toroid can be analogical to H_z component for fiber at the local cross section (their signs only representing the light propagating directions), so, it is the same for H_ρ and H_x, $H_{z'}$ and H_y and the E field components.

For simplicity, we denote $|\phi_i>$ as an arbitrary component of the ith fiber mode and $|\psi_m>$ as the corresponding mth toroid mode. From the Helmhöltz equation for

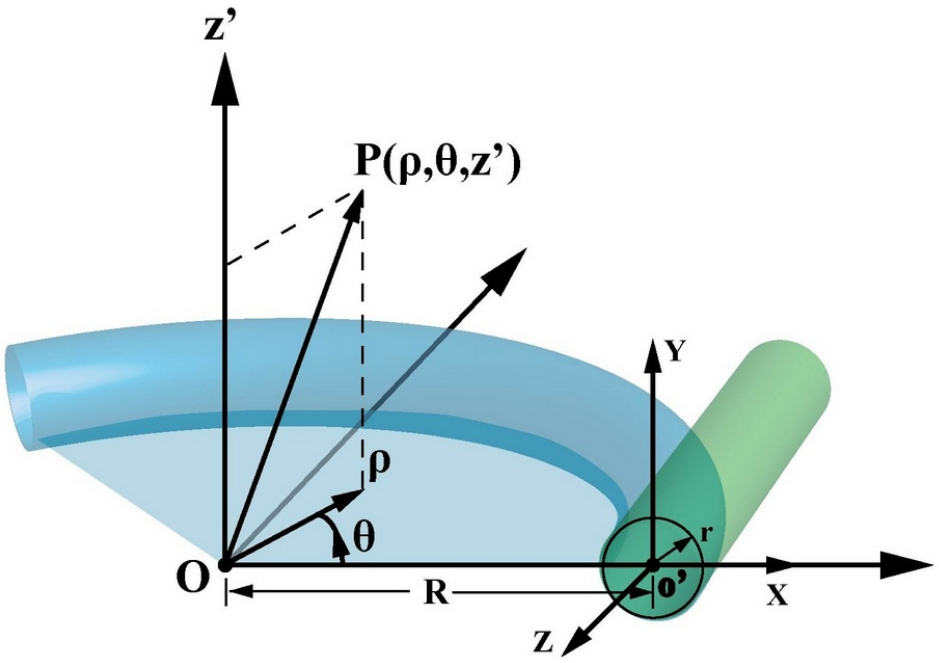

Figure 4.1: The cylindrical coordinate system for microtoroid (blue) and the local cartesian coordinate for fiber (green) with the same core size. The origin of the local cartesian coordinate is located at the center of the toroid ring cross section and the x-direction and y-direction coincide with the radial and axial direction respectively.

a straight fiber in the cartesian coordinate system, we have

$$\widehat{L}_i|\phi_i >= 0, \tag{4.1}$$

where $\widehat{L}_i$ is an operator expressed as

$$\widehat{L}_i = \frac{\partial^2}{\partial x^2} + \frac{\partial^2}{\partial y^2} + (n^2 k_0^2 - \beta_i^2), \tag{4.2}$$

where β_i is the propagation constant of the ith fiber mode. Similarly for a toroid in cylindrical coordinates, we have

$$\widehat{J}_m|\psi_m >= 0, \tag{4.3}$$

where

$$\widehat{J}_m = \frac{\partial^2}{\partial \rho^2} + \frac{\partial^2}{\partial z^2} + n^2 k_0^2 - \frac{m^2}{\rho^2} + \frac{1}{\rho}\frac{\partial}{\partial \rho}. \tag{4.4}$$

Using the relationship between the two coordinates, which we discussed above, it is easy to derive the Eq. (4.5) through comparing the Eq. (4.2) and Eq. (4.4).

$$\widehat{J}_m = \widehat{L}_i + \Delta\widehat{L}, \tag{4.5}$$

where

$$\Delta\widehat{L} = -\frac{m^2}{\rho^2} + \frac{1}{\rho}\frac{\partial}{\partial\rho} + \beta_i^2. \tag{4.6}$$

Assuming $R \gg r$, where R is the toroid major radius and r is the toroid minor radius, the EM field of a toroid can be described as a superposition of straight fiber modes with the same core size

$$|\psi_m >= \sum a_{mi}|\phi_i >, \tag{4.7}$$

where a_{mi} is the weighting coefficient to be determined. Then,

$$\widehat{J}_m|\psi_m >= \sum a_{mi}\widehat{L}_i|\phi_i > + \sum a_{mi}\Delta\widehat{L}|\phi_i > . \tag{4.8}$$

Noting that the LHS and the first term on the right are zero according to Eq. (4.1) and Eq. (4.3), we obtain

$$< \phi_k| \sum a_{mi}\Delta\widehat{L}|\phi_i >= 0. \tag{4.9}$$

Finally, we have a set of homogeneous equations expressed as

$$\Delta\mathbf{L} \cdot \mathbf{V} = 0, \tag{4.10}$$

where $\Delta\mathbf{L}$ is a $N \times N$ matrix with element $\Delta l_{ki} =< \phi_k|\Delta\widehat{L}|\phi_i >$;
$\mathbf{V} = (a_{m1}, ..., a_{mi}, ..., a_{mN})$ is the weighting coefficient vector and N is the number of fiber modes.
The non-zero solutions of $\mathbf{V}$ exit when the determinant $\det(\Delta\mathbf{L})$ satisfies

$$\det(\Delta\mathbf{L}) = 0. \tag{4.11}$$

Assume the light propagates a small distance $dl = \rho(x)d\theta$ due to an increase of the azimuthal angle $d\theta$. The toroid mode will propagate as

$$|\psi_m >' = |\psi_m > e^{jm\theta} = \sum a_{mi}|\phi_i > e^{jm\theta}, \tag{4.12}$$

while the fiber mode will become

$$|\phi_i>' = |\phi_i > e^{j\beta_i z}. \tag{4.13}$$

Using the Taylor expansion, this can be rewritten

$$\sum a_{mi}|\phi_i > (1 + jmd\theta) = \sum a_{mi}|\phi_i > (1 + j\beta_i z), \tag{4.14}$$

or

$$m\mathbf{V} = (\mathbf{R} + \mathbf{X})\mathbf{C}\mathbf{V}, \tag{4.15}$$

where $\mathbf{V}$ is the coefficient vector, $\mathbf{R}$ is a diagonal matrix with elements of toroid major radius R, $\mathbf{X}$ is a square matrix with elements $x_{ki} =< \phi_k|x|\phi_i >$, and $\mathbf{C}$ is also a diagonal matrix with elements of the propagation constants β_i. It can be observed that the weighting coefficient vector is the eigenvector of the eigenfunction Eq. (4.15) and the mode number m are its eigenvalues.

4.1.2 Mode solver based on graded index fiber

The principle of above method is simple but has its limitation. When the waveguide diameter is below the single mode condition that only one guided mode is allowed, this method is no longer applicable. One can instead transfer the cavity loop to an equivalent straight fiber with graded index profile by the conformal mapping, which is similar to the derivation in Ref. [63] for the bent fiber analysis. The only difference of a cavity loop from the bent fiber is that the stress-optic effects are out of the consideration for the refractive index upon bending. This is evident by rewriting Eq. (4.3) in the following form

$$\frac{\partial^2}{\partial\rho^2}|\psi_m > + \frac{\partial^2}{\partial z^2}|\psi_m > + (n^2k_0^2 + \frac{1}{\rho}\frac{\partial}{\partial\rho} - \frac{m^2}{\rho^2} + \beta^2 - \beta^2)|\psi_m >= 0, \tag{4.16}$$

$$\frac{\partial^2}{\partial\rho^2}|\psi_m > + \frac{\partial^2}{\partial z^2}|\psi_m > + (n_g^2k_0^2 - \beta_m^2)|\psi_m >= 0. \tag{4.17}$$

Here, $n_g^2 = n^2 + (\beta_m^2 - m^2/\rho^2)/k_0^2$ and the $\frac{1}{\rho}\frac{\partial}{\partial\rho}$ term is ignored as the small radiation loss. Eq. (4.17) has the same form as that of a straight fiber, and the graded refractive index n_g can be considered as the refractive index profile of an equivalent straight fiber corresponding to a toroid. Hence by solving the mode for a straight fiber whose

refractive index profile is defined by n_g, one can maximize the mode overlap between the toroid mode to be considered and the fundamental mode of the graded index fiber. This enhances the computation efficiency significantly comparing to the above proposed expansion on a set of straight normal fiber modes.

Given the azimuthal mode number of a toroid expressed as

$$m = \frac{2\pi R_{eff} n}{\lambda} = \beta R, \tag{4.18}$$

where R is the toroid major radius and λ is the wavelength of light, the equivalent fiber refractive index can be simplified as

$$n_g = \sqrt{n^2 + \frac{m^2}{k_0^2}(\frac{1}{R^2} - \frac{1}{\rho^2})} = n\sqrt{1 + \frac{\rho^2 - R^2}{\rho^2}}. \tag{4.19}$$

In the extreme case of a toroid with infinite major diameter, the refractive index profile of the corresponding graded fiber is identical to a step index fiber as expected. The refractive index profiles for bent fiber and toroid are very close when using the same structure parameters, especially inside the core where most of the propagating power is located. With a little effort to modify the mode solver for a normal straight fiber, we can get the toroid mode profiles with high accuracy.

4.1.3 Radiation Loss

In addition to the cavity mode profile obtained from the above method, one may also estimate the corresponding quality factor (Q) in high accuracy. As known the overall quality factor is determined by material absorption, radiation loss, surface contamination and defects. In particular, radiation quality factor Q_{rad} is a characterization of radiation loss due to the bending nature of the cavity surface. It dominates the loss for cavities with small radius of coverture. Similar to the radiation loss analysis of a bent fiber, the radiation Q is defined by

$$Q_{rad} = 2\pi f_{res} E_{store}/P_{rad} = 2\pi f_{res} \frac{2\pi R n_{core}}{c} \frac{P}{P_{rad}}, \tag{4.20}$$

where f_{res} is the resonant frequency of the toroid; E_{store} is the energy stored in the toroid; P_{rad} is the radiation loss power; n_{core} is the refractive index of the core; c is the speed of light in free space; and P is the propagation power inside the toroid.

In order to calculate the Q_{rad}, we can compute the power from Poynting vector and obtain

$$P = \int_{cross} \mathbf{S}_z d\mathbf{a} = \int_{cross} (\mathbf{E}_x \mathbf{H}_y^* - \mathbf{E}_y \mathbf{H}_x^*) d\mathbf{a}, \tag{4.21}$$

while the radiation loss power is calculated by the volume current method [62]. Using this method, the electric field inside the dielectric toroid is processed as current on an antenna of infinitesimal thickness. The far field can be specified from this current. Thus, the radiation power is determined by calculating the Poynting vector of this far field.

From the Maxwell's equations without source, we have

$$\nabla \times \mathbf{H} = -i(\frac{\epsilon_0}{\mu_0})^{1/2} k n^2 \mathbf{E}, \tag{4.22}$$

where, $k = \frac{\omega}{c} = \omega\sqrt{\epsilon_0 \mu_0}$ and $n = \sqrt{\epsilon_r}$.

This leads to the equivalent antenna current distribution

$$\nabla \times \mathbf{H} = \mathbf{J} - i(\frac{\epsilon_0}{\mu_0})^{1/2} k n_{cl}^2 \mathbf{E}. \tag{4.23}$$

and

$$\mathbf{J} = i(\frac{\epsilon_0}{\mu_0})^{1/2} k (n_{cl}^2 - n^2) \mathbf{E}, \tag{4.24}$$

where $\mathbf{E}$ is the exact field of the fiber and n is its refractive index profile,

$$n = \begin{cases} n_{co} & r' < \rho \\ n_{cl} & r' > \rho. \end{cases} \tag{4.25}$$

As $\mathbf{J}$ is nonzero only within the volume corresponding to the fiber core, we can approximate $\mathbf{E}$ by the local mode field, i.e. by the field of a uniform fiber in local regions, provided the bending radius is large enough to satisfy

$$R = R_c/\rho \gg 4\pi V/\{(2\Delta)^{1/2} \tilde{W}^2\}, \tag{4.26}$$

where R_c is the bending radius, ρ is the core radius, $V = (U^2 + W^2)^{1/2} = [\rho^2(k^2 n_{co}^2 - \beta^2) + \rho^2(\beta^2 - k^2 n_{cl}^2)]^{1/2} = k\rho(n_{co}^2 - n_{cl}^2)^{1/2} = k\rho n_{co}(2\Delta)^{1/2}$ and $\tilde{W} = \rho(\tilde{\beta}^2 - k^2 n_{cl}^2)^{1/2}$. U is called the core parameter and W is called the cladding parameter for bound modes.

Next, taking the advantage of the large ratio of bend to core radius and that the direction of $\mathbf{J}$ does not vary over the cross-section, we suppose that the distribution of currents through the core cross-section is concentrated on the fiber axis, resulting in a line current $\mathbf{I}_a$ defined by

$$\mathbf{I}_a = \hat{\mathbf{n}} \int_{A_{co}} J dA, \tag{4.27}$$

where J is the magnitude of $\mathbf{J}$, A_{co} is the core cross-section area and $\hat{\mathbf{n}}$ is a unit vector parallel to a fixed direction in the fiber cross-section. With the weak-guidance approximation, the power radiated is insensitive to polarization, since $R_c \gg \rho$. One can assume that the transverse electric field is parallel to the z-axis in cylindrical coordinates, orthogonal to the plane of the bend.

To calculate the power radiated, we follow the far-field expression for vector potential

$$\mathbf{A} = \frac{\mu_0}{4\pi s}\mathbf{M} exp(iksn_c l) \tag{4.28}$$

$$\mathbf{M} = \int_v \mathbf{J}(\mathbf{r}') exp(-iks' n_{cl} cos\chi) dV', \tag{4.29}$$

where V is the volume occupied by the currents and $s = |\mathbf{r}|$. The far-field point is described by a spherical polar coordinates (s, θ, ϕ), whose original point located at the center of toroid. We can deduce the vector to only contain the z-component

$$M_z = 2\pi R_c I_c J_\nu (kR_c n_{cl} sin\theta), \tag{4.30}$$

where $\nu = \beta R_c$, $cos\chi = sin\theta cos(\phi - \phi')$ and χ is the angle between s and s'.

The total radiated power is

$$\begin{aligned} P_{rad} &= \frac{c^2 k^2 s^2 n_{cl}}{2} (\frac{\epsilon_0}{\mu_0})^{1/2} \int_{s_\infty} |\hat{\mathbf{r}} \times \mathbf{A}|^2 d\Omega \\ &= \frac{k^2 n_{cl}}{32\pi^2} (\frac{\mu_0}{\epsilon_0})^{1/2} \int_0^{2\pi} \int_0^{\pi} \{|M_\theta|^2 + |M_\phi|^2\} sin\theta d\theta d\phi. \end{aligned} \tag{4.31}$$

Since $M_\theta = -M_z sin\theta$ and $M_\phi = 0$ in our case,

$$P_{rad} = \frac{\pi R_c^2 k^2 n_{cl}}{4} (\frac{\mu_0}{\epsilon_0})^{1/2} |I_c|^2 \int_0^{\pi} |J_\nu (kR_c n_{cl} sin\theta)|^2 sin^3\theta d\theta. \tag{4.32}$$

4.2 Results

All the modes are calculated with the same parameters. The refractive index of the fiber core or toroid is 1.4457 for silica, and the cladding or outside toroid is 1.0 for air. The fiber core radius or toroid minor radius is 2.0 μm, and the bending radius of fiber or toroid major radius is 30 μm. The resonance wavelength in toroid is around 1550 nm. We calculate the straight fiber modes with the finite element method (FEM).

Given the modes of a straight step index fiber, the weighting coefficients are not difficult to calculate according to Eq. (4.15). All of the fiber modes are normalized based on the transverse magnetic field, as they are continuous in the piecewise homogeneous dielectric toroid. Once the weighting coefficient vector is determined, the corresponding toroid mode can be calculated according to Eq. (4.7). We can find that both of the two methods can generate the new mode profiles very close to the corresponding toroid modes. As we discussed above, the graded index fiber mode should be more efficient than the step index fiber modes to generate the toroid mode. As expected, the fundamental mode profile of the graded index fiber is more close to that of the toroid, that means the graded index fiber constructs a toroid with higher accuracy than the step index fiber.

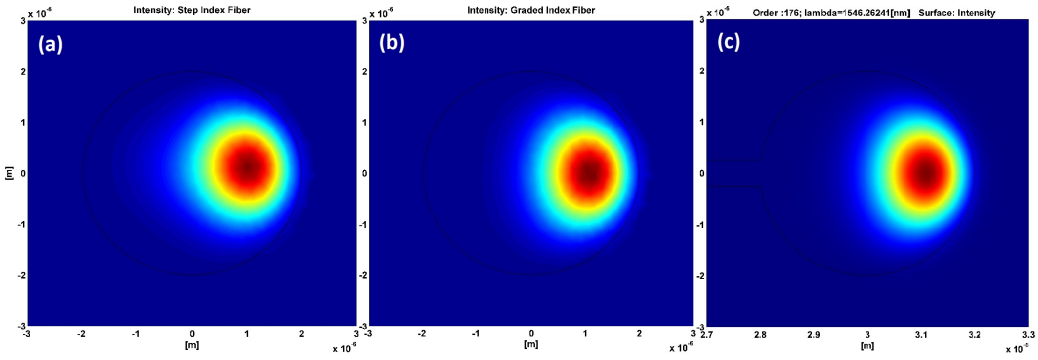

Figure 4.2: Intensity profiles for the fundamental toroid mode from (a) the normal step index fiber modes; (b) a straight graded index fiber; (c) a direct FEM toroid mode solver.

For comparison, we plot the propagating power of the different fundamental toroid modes generated from the step index fiber modes superposition, a straight fiber with graded index profile and a direct toroid mode solver from previous FEM implementation by [43] in Fig. 4.2. From this figure, we can find that the three mode profiles

worked out by different solvers have the identical pattern shape. In order to present it in a quantified way, we define an overlap factor to describe how close one fiber based mode is to the direct FEM implemented toroid mode. The overlap factor is defined by

$$f = \frac{< \varphi | \psi >}{\sqrt{< \varphi | \varphi >< \psi | \psi >}} \tag{4.33}$$

where $|\varphi >$ represents any fiber based mode and $|\psi >$ represent the direct FEM toroid mode. Fig. 4.3 illustrates the trend of the overlap factors with regards to number of normal straight step index fiber modes considered to construct a toroid mode. Clearly, the overlap factor gets closer to the unit as more fiber modes are taken into considerations. The results are convergent and become stable fast within ten modes. The similarity between the fundamental mode from the step index fiber and that from the direct toroid mode solver is close to 98.587% with the contribution of twenty guided fiber modes.

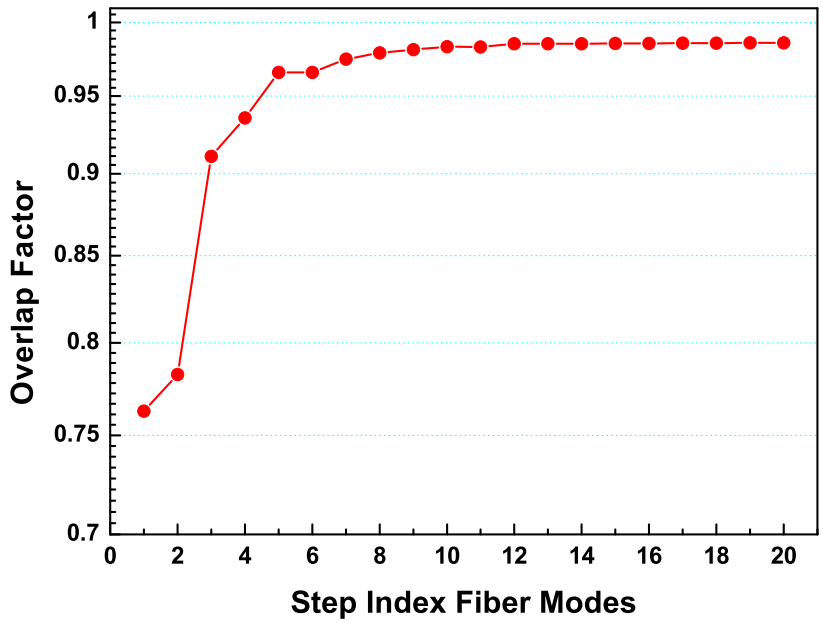

Figure 4.3: The overlap factors for the mode solver based on a set of straight step index fiber modes with increasing mode numbers. With the increasing number of considered fiber modes, the trend of the overlap factor becomes convergent and stable.

Comparing to the previously reported FEM implementation [43], the simplicity and efficiency of the new method are quite distinct. The computation for the toroid modes is greatly reduced with the fiber modes at hand, as there are methods that can calculate the straight fiber modes analytically. With these analytic solutions the computation of the toroid modes becomes accurate and efficient. The computational time can be reduced to half by the new mode solver comparing with the direct FEM toroid mode solver.

However, as we known, there is only one guided mode in a fiber, when the normalized frequency V defined by Eq. (3.1) is smaller than 2.405 [56]. Meanwhile, Fig. 4.3 indicates that the accuracy of this method drops rapidly when the number of fiber modes is below ten. For a cavity structure that can only support insufficient modes, the graded index fiber mode solver is a better solution. The overlap factor of the fundamental mode based on the graded index fiber with respect to the direct toroid mode is 99.961%. This value is better than that from the step index fiber modes. Besides, only one mode needs to be calculated from the straight fiber mode solver with graded index profile, as people are interested in the fundamental WGM cavity mode in most cases. In contrast to calculating dozens of modes, it reduces the computational resources and time considerably, although it requires several iteration processes.

One point about the mode solver based on the graded index fiber that needs to be emphasized is the ignoring of the radiation loss in a cavity. This assumption is only valid for the high Q WGM cavity. Since the power loss due to the radiation is one hundred millionth of the total power circulating within the cavity, there is no noticeable change to the mode profile under this assumption. When the bent is too large and causes considerable radiation loss, the enhanced loss term leads to the decreasing of the simulation accuracy.

The radiative quality factor Q_{rad} is calculated from toroid modes based on all the three solvers by the volume current method. We calculate the Q_{rad} for a set of toroids with different structure parameters, such as the minor diameters chosen in the range of [0.8 μm, 3.2 μm] and the major diameters chosen as 40 μm, 60 μm and 80 μm. All of the calculated results are shown in Fig. 4.4. As the minor diameter increases, the Q_{rad} increases as well and becomes less sensitive to the change of the size for all three different major diameters. This confirms that the radiative loss is dominant for small size toroid, and becomes negligible for big ones.

Additionally, Fig. 4.4 illustrates that the three mode solvers provide the identical

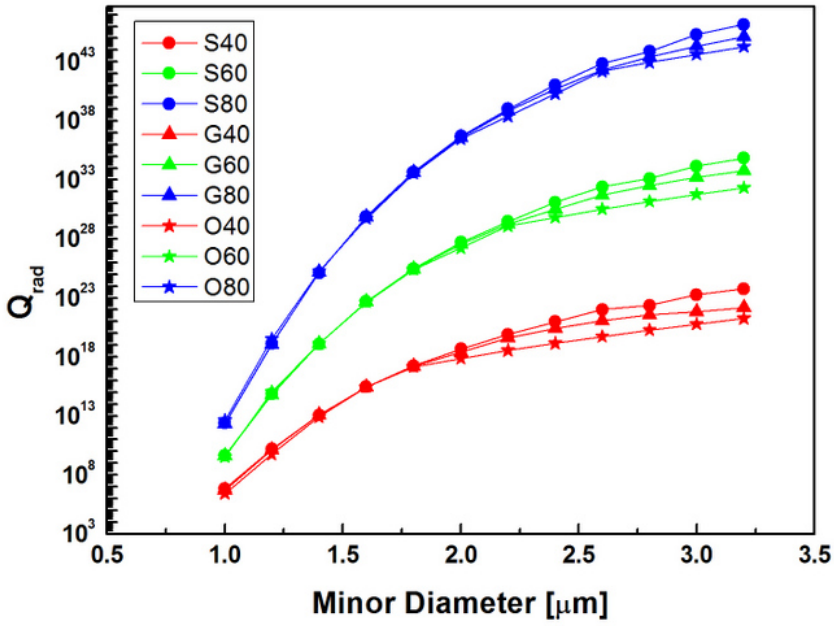

Figure 4.4: Q_{rad} calculated from the direct FEM toroid mode solver (Stars) , the step index fiber modes superposition (Circles) and the graded index fiber modes (Triangles). The results for toroids with different major diameters are distinguished by symbol colors. The red, green and blue sets represent the 40 μm, 60 μm and 80 μm major diameter toroids respectively.

modes from another angle. The radiation quality factors have the same values for the toroids with smaller minor diameters. They become divergent when the minor diameters get larger. Because of the weaker confinement on the mode pattern from larger minor diameters, the distortion of the mode profiles due to the bending is magnified. The difference of the simulation results is induced by the different ways to dealing with the bending. Consequently, the disparity is more distinguishable for the cavity ring with higher curvature value. For toroid cavities, the ones with smaller major diameters are easier to exhibit this difference subjected to the same confinement from the minor diameters.

4.3 Conclusion

One method with high efficiency and accuracy for toroid mode solving has been claimed and used to calculate the radiative quality factor. The method is developed on the high similarity between a toroid and a bent fiber. However, this method is not restricted to a toroid geometry. Any axial-symmetric resonator's mode can be solved by this method, such as microring, microsphere and microdisk. The radiative Q factor is calculated by the volume current method which is widely used to calculate the bending loss of a fiber. We confirm that the radiative loss is only dominant for toroids with small sizes.

Chapter 5

Experiments

5.1 Fabrication of Chip Based Cavity

5.1.1 Microsphere Reflow

We fabricate microspheres successfully with both of the SM600 and SMF-28 optical fibers. The former is designed for the single mode propagating of 600 nm laser source, while the later is for the commercial optical communication at the 1550 nm wavelength which is much more affordable. The microsphere cavity is reflowed on a supporting stem through fusing the tip of a fiber with a high power CO_2 laser. Due to the high absorption at 10.6 μm wavelength, the silica fiber tip melts under the focused laser. The surface tension ensures the spheroidal profile when the silica is melting and the smooth surface when it cools down to the solid state, with the sufficient power and balanced spatial intensity distribution of the laser beam. Fig. 5.1 shows our reflow system for the WGM cavity fabrication. The system is sitting on an optical table to avoid the vibrations. The CO_2 laser is controlled by the controller on the shelf which is connected by a function generator. Thus, we are able to shoot the fiber tip with either a continuous wave or an arbitrary laser pulse. The fiber is clamped on the holder far enough away from the laser source. Out of a certain distance, the laser beam is approximately considered as a plane wave and focuses on the fiber tip through a condense lens. At the end, the beam is absorbed by the beam block for safety.

Limited by beam spot size of the CO_2 laser, the diameter of original fiber with cladding is too big, due to the high requirement of the fusing power distribution on the tip. Besides, the big cavity dimension results in a large mode volume, which has

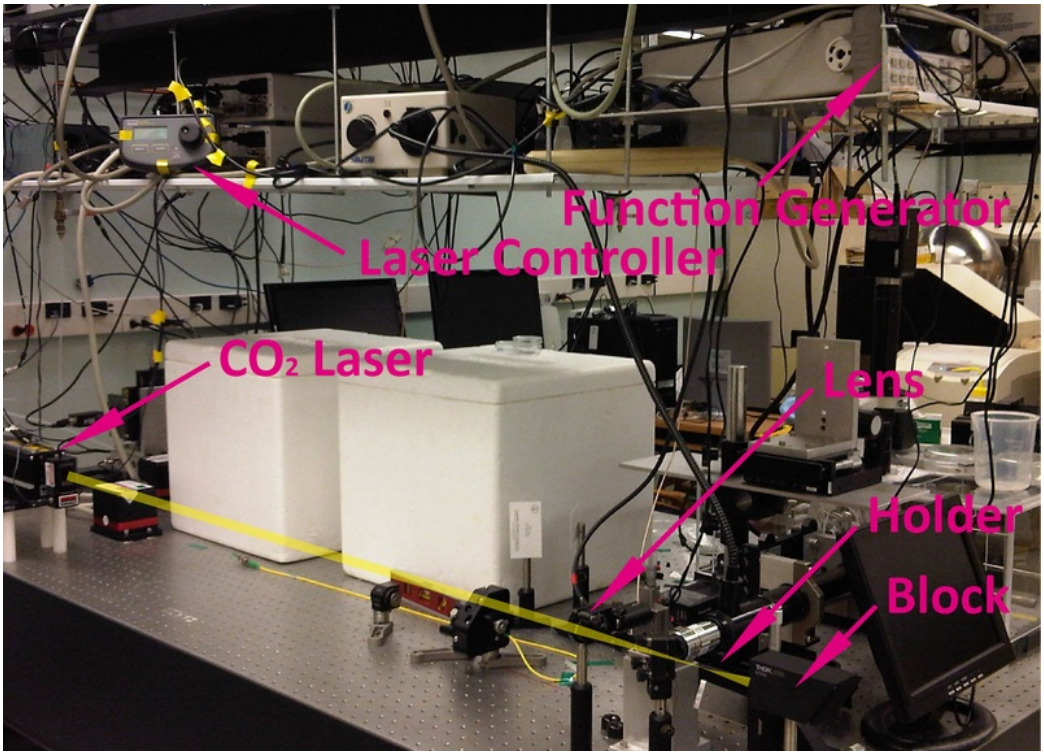

Figure 5.1: The reflow system for cavity fabrication. This system can fuse microspheres or microtoroids with a few modifications.

a negative contribution to the sensitivity. To get a microsphere within a controllable size range, the striped fiber is etched by buffered hydrogen fluoride (HF) before the reflow. Before etching, one length of the optical fiber is tripped and cleaned with IPA, since the polymer jacket is an obstruction to the etching. For a SM600 optical fiber, the diameter of the bare cladding is 128 μm. A bunch of striped fibers are immersed in the buffered HF solution. During the etching process, some of the fibers with different etching periods are selected for the SEM measurement. The HF etches the silica fiber isotropically and results in a smooth surface (Fig. 5.2). Comparing all the measured samples, we find the etching rate with respect to the time is a constant. Therefore, the final dimension of an etched fiber is easy to control by the etching time according to the relation shown in Fig. 5.3.

An alternative solution is to use a tapered fiber, which undergoes the similar procedure as the taper coupler. The suitable taper for a good cavity is smaller than the original fiber but bigger than the taper for coupling, so the pulling stops when the desired diameter is reached. Then, cleaving at the center of the pulling section provides two identical tapers. The former method can massively produce fiber stems

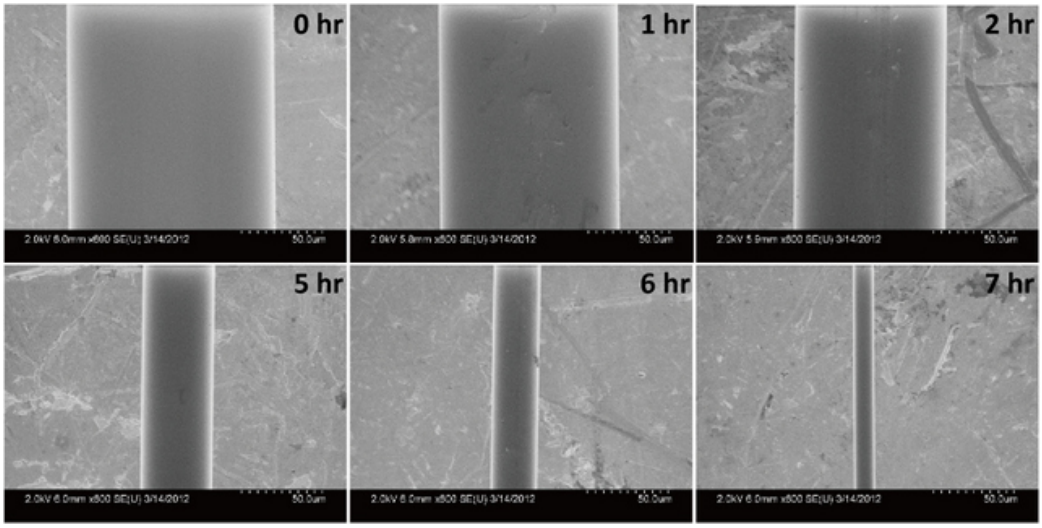

Figure 5.2: SEM micrographies of the original fiber and ones with different etching hours.

with unform size in a few hours, while the later can only pull one length of fiber at one time but it only takes a few minutes. Considering our lab setup, we choose the later one, which is environment friendly that its only byproduct is H_2O.

Both of the continuous and pulsed laser beams are able to fuse the fiber tip into a spherical cavity. For a continuous wave, one needs to keep the fusing power low and heat the silica slowly to melt down. If the power is two high and the temperature goes up too fast, the melting silica can not stay and accumulate at the tip to form a sphere. Like the taper pulling, it needs the experimenter to monitor the fusing process and control the fusing time. On the other hand, the laser pulse needs a high power and a short time period to melt the silica and form a sphere. If the beam power is not high enough, the final silica sphere becomes eccentric when it cools down. The ellipticity leads to more radiative loss and smaller Q to a spherical cavity. Considering the controllability, repetitiveness and stability of the fusing process, our WGM cavities are fabricated with laser pulses.

5.1.2 Microtoroid Reflow

The reflow of the microtoroid from a microdisk is more restrictive than that of the microsphere. The cross section exposed to the laser beam is larger than fiber taper. At the same time, it is more sensitive to the spacial distribution of laser intensity. In order to make an axial symmetrical toroid cavity, we want the silica disk edge to

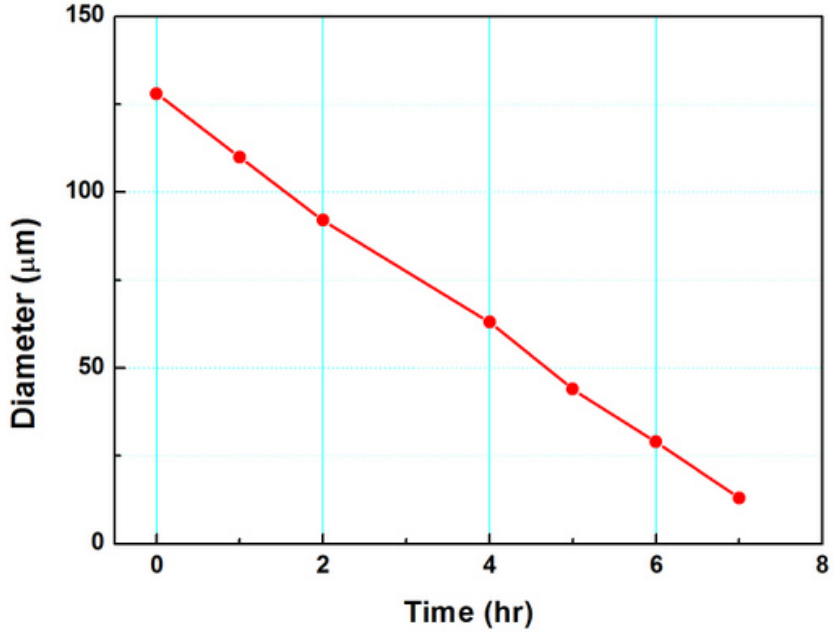

Figure 5.3: The relation of measured fiber diameters with respect to the etching time. It shows that the fiber diameter is inversely proportional to the HF etching time.

melt, shrink and cool down simultaneously during a single pulse period. Any small aberration will cause the imperfection of the toroid shape and lower the quality factor considerably, since its mode volume is highly confined in the silica ring in both radial and axial directions and the mode pattern is more sensitive to the geometry than microsphere. One more attention should be paid to the toroid reflow is the beam incident angle. Instead of a 1D fiber taper, the 2D disk is much more sensitive to the angle of incident laser beam. Therefore, people must align the beam and the disk sample carefully and make the beam perpendicular to the disk plane, otherwise the fused toroid will be tilted. This leads to the strong radiation loss and scattering loss at the surface, and a low quality factor as well. Besides, the reflow power becomes more critical to microtoroid. The silica disk does not totally melt if the power is too low, which leads to a small toroid ring and high radiative loss. On the other hand, the extra silica sputtered to the ring surface from the center area causes the increasing of scattering light when it is over heated.

The position, where we put the taper or disk, for reflow is another important factor. We put both near the focal point of the condense lens. This is the most

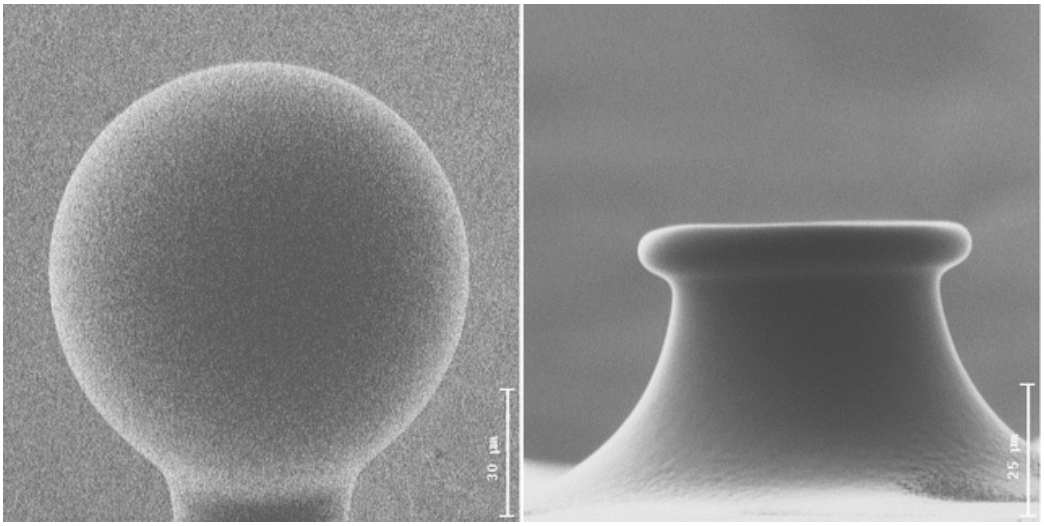

Figure 5.4: The focused ion beam (FIB) images of fabricated WGM cavities. A silica microsphere (left) sitting on a fiber stem. Its diameter is around 100 μm. A silica microtoroid (right) supported by a silicon pillar. Its major diameter is around 65 μm.

efficient fusing position because of the highest laser intensity at the focal point. The exact fusing positions for microsphere and microtoroid are a little different, since the beam spot size needs to match the profile of the taper or disk. From our experience, the effect of the fusing position is more notable to the cavity quality factor than that of the fusing power. We find that the Q of a cavity drops by more than two orders when it is fused at a position 0.2 mm away from the optimized one. On the other hand, it is relative tolerant to the power changing. We do not see any large drop of the Q within $\pm 5\%$ fluctuation of the fusing power. Fig. 5.4 shows the pictures of our reflowed high Q microsphere and microtoroid, which are taken by the focused ion beam (FIB). The quality factor of the WGM cavity is around 2×10^8 for the microsphere and roughly 5×10^7 for the microtoroid at 630 nm wavelength. The current record of Q we have gotten is $(4.7 \pm 0.1) \times 10^8$ for a microsphere with 100 μm diameter at 630 nm.

5.2 Q Measurement

When a WGM cavity has been fabricated, we move it into the measuring setup which is fixed on the optical table. The whole setup, including the cavity and taper, is in a sealed box which can block most of the interference from the environment. The measurement can be affected by any small fluctuations, such as dust, vibration or

air flow, because of the high sensitivity of the cavity. As it is illustrated in Fig. 5.5, the taper holder is sitting on a fixed aluminum plank. Meanwhile, the cavity is on a movable cantilever. There are three micrometers to move the cantilever in X, Y and Z direction respectively. When it is in a good posture for coupling, a nanocube under the cantilever is used to adjust the distance between cavity and taper in a more subtle way. Two microscopes provide the top and side view images in real time. Therefore, we are able to tune the coupling condition from overcoupling to undercoupling region. As we discussed before, the intrinsic quality factor of a cavity is measurable in the very weak undercoupling region.

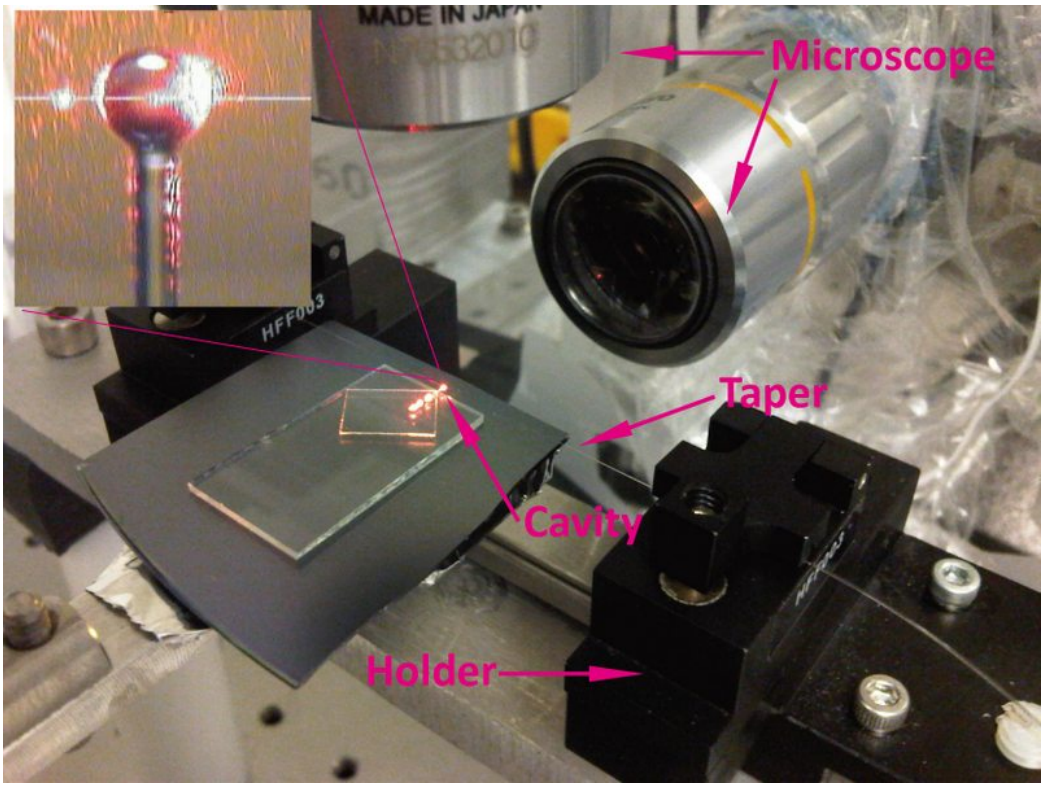

Figure 5.5: The setup for the measurement. One spherical cavity is coupling with the taper. The distance between them is controlled by a nanocube under the cavity holder. Insert: The top view of the coupling between the taper and microsphere from the microscope.

We send a triangular wave signal from the function generator to the laser controller to modulate the input laser frequency. The frequency modulation voltage is set to be 1 V at the frequency of 100 Hz. The frequency modulation parameter of the controller is 0.027 nm/V. Then, the red laser continuously scans its wavelength in a 0.027 nm

range near 630 nm. One photodetector records the transmission output from the tapered fiber coupler and displays it on the oscilloscope. As what we know from the theory, the Lorentz dip comes on the spectrum when the scan passes through the resonant wavelength.

Fig. 5.6 shows a general transmission output from the fiber taper. A spherical cavity is coupled with the taper, which has a lot of resonant modes in the scan range. The green signal is the output intensity. Each dip on it represents a whispering gallery mode in the cavity. The yellow one is the frequency modulation signal. As the signal is scanning up and down, the transmission has a periodic output at the scan frequency. The transmission spectrum is symmetric with respect to the turning point for the modulation.

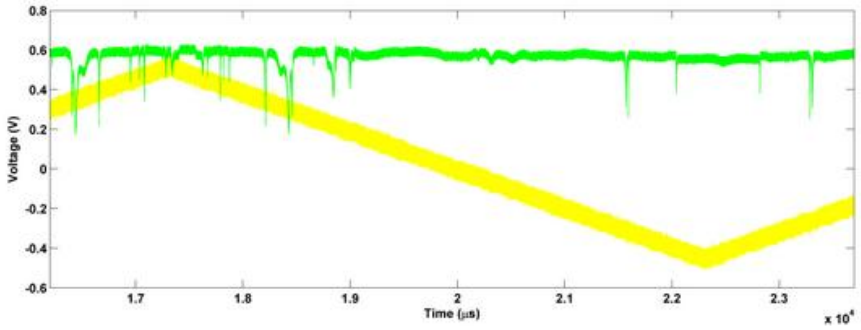

Figure 5.6: Spectrum of a microsphere touched with the taper. Each resonant mode of the cavity shows a dip on the spectrum. The broader dips are overcoupled modes.

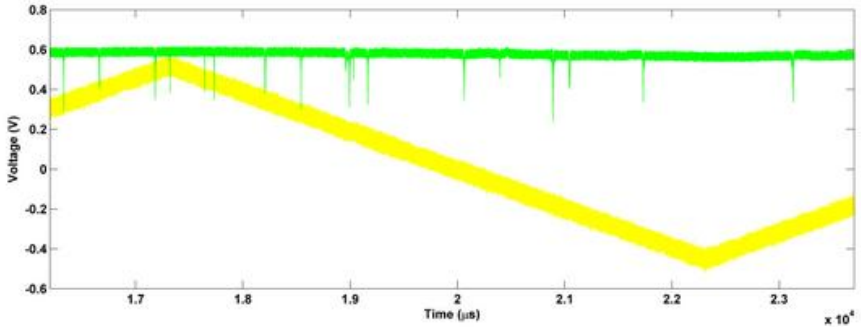

Figure 5.7: Spectrum of a microsphere coupled with the taper but without touching. All the resonant modes are under coupled.

When a cavity is moving toward the taper, the evanescent field will attract the tiny taper because of the Van der Waals force and optical gradient force [65]. The optical

gradient force is also the foundation of the optical tweezers [66]. It always pushes a dielectric particle in an optical field to the high intensity area and is proportional to the gradient of the field. As illustrated previously, the evanescent field tail decays exponentially outside the cavity boundary at the equator, which creates a strong optical gradient force to push the dielectric taper toward the cavity surface. It is able to attract the atoms and virus as well [67, 68], when they diffuse into the evanescent field. This property increases the sensing efficiency of the WGM cavity in a very low concentration solution. If the cavity is contacting with the taper, some of the resonant modes are under the over coupling condition, because they are getting too close. Therefore, one finds some of the resonant modes in the spectrum with much broader linewidthes than the others. The strong coupling loss due to the over coupling lowers the total quality factors for those modes.

As in the over coupled region, the resonant linewidth is significant broadened, we can never measure the intrinsic quality factor accurately for a cavity. In order to get a accurate value, we carefully tune the nanocube to generate a small gap between the cavity and the taper. This leads to all the resonant modes under coupling with the taper. Comparing Fig. 5.7, which is the transmission of the undercoupled microsphere, with Fig. 5.6, the transmission is more smooth due to the less coupling influence. Some undercoupling modes in the touched condition disappear when the taper becomes untouched. The previous overcoupling modes become undercoupling and reduce the linewidth for the measuring.

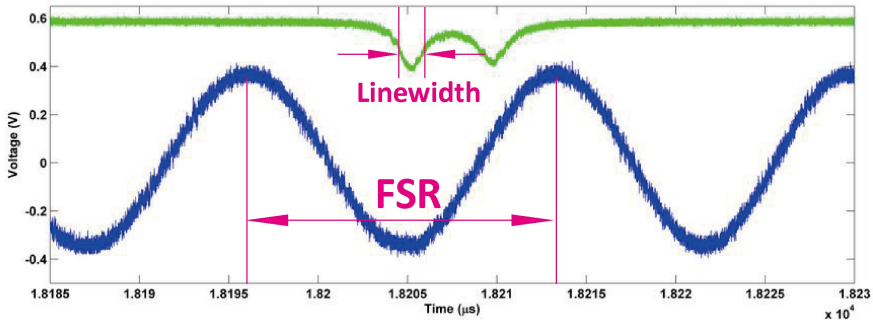

Figure 5.8: The resonant linewidth of a microsphere. The two dips represent the split of forward and backward propagation modes in a WGM cavity. The blue signal is generated from the reference interferometer. The free spectral range (FSR) of the interferometer is 36 MHz and the Q calculated based on it is $(1.9 \pm 0.1) \times 10^8$.

Fig. 5.8 is a partial enlarged view of the resonant dip of the undercoupled microsphere transmission. Here we find that the resonant dip is actually composed of

two different resonant frequencies. They are the splitting modes due to the opposite directional propagating light in the WGM cavity. It is not detectable in the low Q WGM cavity, because the two resonant frequencies are so close that they merge into a single dip when the linewidth is comparable or larger than the split. The split frequency is able to give some additional information of the sensing particle, such as the size [69].

One additional point about the high Q measurement is the influence of laser noise. The laser frequency has some certain fluctuation which is negligible usually. However, we can never neglect this noise when the Q is above 10^8. Since the laser frequency does not change linearly according to the modulation signal due to the fluctuation, the Q calculated based on the modulation signal is no longer accurate for high Q WGM cavity. Therefore, we use an optical interferometer to cancel out the laser noise. The free spectral range (FSR) of the interferometer is 36 MHz. According to the single period of quasi-sinusoidal signal from the reference interferometer and the time span of the resonant linewidth in Fig. 5.8, we work out the quality factor is $(1.9 \pm 0.1) \times 10^8$ for this spherical WGM cavity.

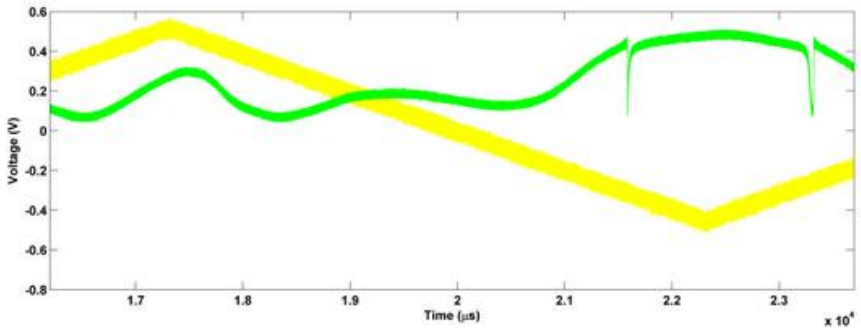

Figure 5.9: Spectrum of a microtoroid touched with the taper.

Fig. 5.9 and 5.10 are the transmission spectrums of the microtoroid. One distinct feature of the toroid spectrum is its neatness. Different from the microsphere, it has only one or two resonant modes in the scan range even when it is touched with the taper. One reason is that the toroid is smaller than the sphere. So, the microtoroid has a larger free spectral range and smaller azimuthal mode number. The other is its additional confinement along the axial direction. This is one of the advantages for the microtoroid as a sensor. When the resonant frequency is shifting due to a binding event, one will not confuse the shift with the neighboring resonant mode.

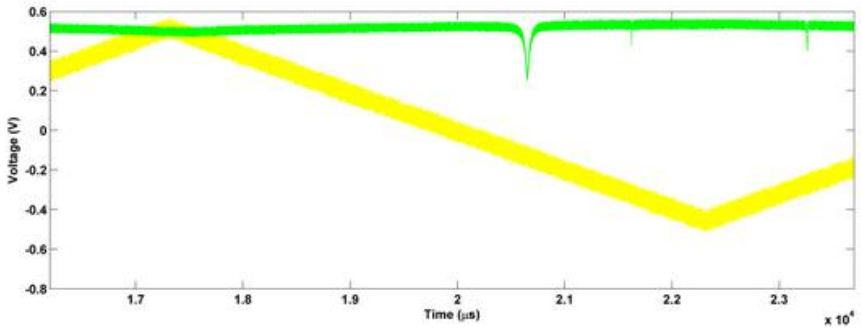

Figure 5.10: Spectrum of a undercoupled microtoroid without touching. There are only one high Q mode and one low Q mode.

5.3 WGM Sensing Principle

When a small particle moves close to the cavity, it changes the local EM field distribution. This leads to a red shift of the resonant frequency for the cavity, since the changing of the optical path. Detecting this frequency shift works as the basic principle of the WGM sensing.

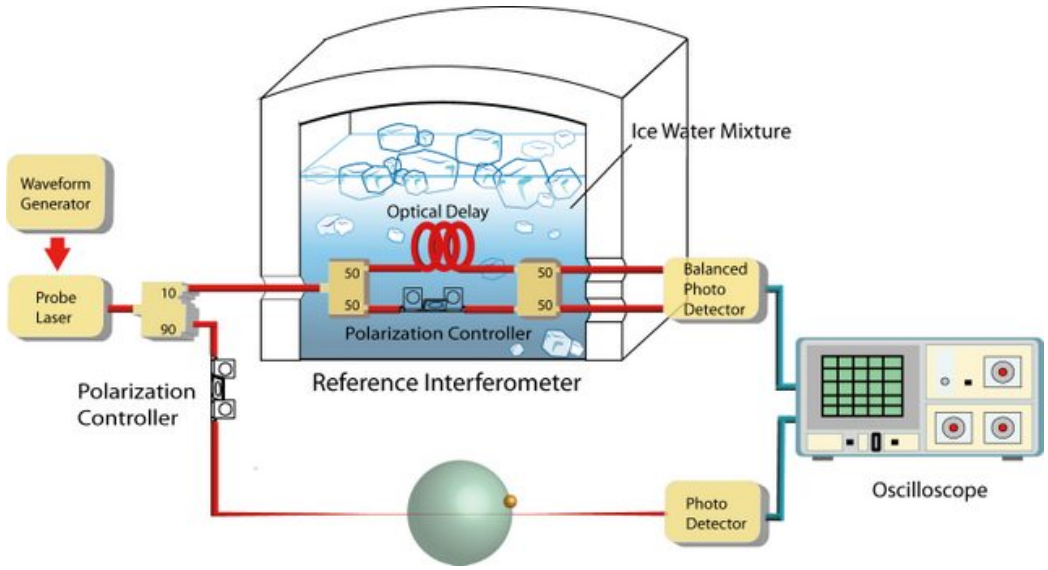

Figure 5.11: The schematic drawing of the measuring system for the binding event. The interferometer is used to wash out the laser noise and increase the measuring accuracy. When a particle moves into the evanescent field, a shift of the resonant frequency appears on the oscilloscope.

Fig. 5.11 is a schematic drawing of our measuring system. The 90/10 coupler splits the modulated laser into two beams. Ninety percent of the laser passes through the taper and couples with the cavity in an aqueous environment. The rest goes into a temperature stabilized reference interferometer. Combining these two signals into an oscilloscope, we measure the resonate frequency and its sift due to the binding accurately [1]. The cavity and taper are both submerged in buffered solution contained in a home made cell. Solutions with different particle concentrations are injected into the cell for testing.

For those small particles we are interested in, such as a virion or single protein, their dimensions are below 100 nm. Comparing to the mode volumes of WGM cavities which are around serval hundred μm^3, the particle size is so small that it is reasonable to treat the influence of small particles as a perturbation to the micro-

cavity system. Therefore, using the first order perturbation theory, we work out the resonant frequency shift due to the binding of a single particle to be[1]

$$\delta\omega = -\omega_0 \frac{\delta\epsilon_r |\mathbf{E}(\mathbf{r})|^2 V_p}{2\int \epsilon_r |\mathbf{E}|^2 dV}, \tag{5.1}$$

where ω_0 is the resonant angular frequency, $\mathbf{E}(\mathbf{r})$ is the electric field at the particle position which is considered as a plane wave, $\delta\epsilon_r$ is the refractive index difference of the particle to its aqueous environment, V_p is the particle volume and the denominator is an integral over the whole space. The minus sign means the shift of the resonance toward the lower frequency or larger wavelength.

The shift signal from the perturbation is only detectable when it is comparable or larger than the resonant linewidth. So the sensitivity of WGM sensing is proportional to the ratio of the frequency shift $\delta\omega$ to the resonant linewidth $\Delta\omega$. Recall the definition of a WGM cavity mode volume Eq. (2.51) and the quality factor with the linewidth Eq. (3.27), so we obtain

$$\left|\frac{\delta\omega}{\Delta\omega}\right| = \frac{\delta\epsilon_r V_p Q}{2V_m} \frac{|\mathbf{E}(\mathbf{r})|^2}{|\mathbf{E}_{max}|^2}. \tag{5.2}$$

Consequently, we want to maximize the value of Eq. (5.2) to achieve the high sensitivity. $\delta\epsilon_r$ and V_p are determined by the particle, so they are not under our control. Obviously, the smaller index difference and size of the particle make it more difficult to be detected. The equation confirms that the sensitivity is proportional to the quality factor of a WGM cavity and inversely proportional to its mode volume V_m. The high Q cavity functions as an amplifier to magnify the sensing signal by Q, however we have reach the limit of Q at the present time for the fused silica cavity. Although we can further reduce the mode volume by compressing the cavity, it is not necessarily helpful to the sensitivity improvement. The reason is that keeping reducing the cavity size leads to an increasing of the loss from radiation. Smaller cavity has a larger curvature. When the curvature is too large, it weakens the cavity ability to confine light and lowers the quality factor. Minimizing the cavity size to reduce the mode volume beyond certain point will damage the sensitivity rather than improve it. Therefore, we turn to the intensity of the field, $|\mathbf{E}(\mathbf{r})|$ and $|\mathbf{E}_{max}|$, for the improvement method, which is either increasing the field intensity at the particle

[1]Check the details in appendix.

position or decreasing the maximum intensity.

Since the particle presents in the evanescent field tail near the equator, we need to transfer more optical power into this region to enhance the shift signal. From Fig. 2.9, we already know that the WGM field pattern along the radial direction obeys the modified Lorentz distribution. It is impossible to modify the maximum intensity and evanescent field independently for current WGM cavity. In other words, the $|\mathbf{E}(\mathbf{r})|$ and $|\mathbf{E}_{max}|$ increase or decrease simultaneously while the ratio of these two terms does not change. For better sensitivity, we need to modify the current cavity structure so that change the ratio. Fortunately, we are able to greatly enhance the evanescent field without changing the maximum intensity of the whispering gallery mode by implementing the surface plasmon on the cavity surface [70]. This localized surface plasmon resonance (LSPR) are predicted to enhance the frequency shift by several hundred times or even larger for smaller particles.

5.4 WGM Cavity Adorned Metallic Nanostructures

The surface plasmon resonance is another optical sensing mechanism used for measuring the chemical or biological analyte besides the WGM sensing [10]. Since the LSPR leads to the localized strong evanescent field near the metal surface, we want to implement it on our WGM cavity to enhance the sensitivity. Recently, a few attempts have been made on this direction. One is to grow the nanoparticles on the cavity surface chemically [71]. In this method, the cavity has to experience several different kinds of chemical solutions for the reactions. Finally, the cavity is coated with metallic nanorods and nanospheres [17]. However, either the residues in those solutions for chemical reactions or the superfluous metallic particles results in the strong optical loss and very low quality factor. Another method is using a metallic nanobeads solution and making the beads to randomly diffuse onto the cavity surface at a very low concentration [19]. Although the Q is acceptable, around 5×10^5, the deposition position is highly uncontrollable. Besides, the diffusion in solution is very time consuming and the cell needs to be rinsed carefully before the real sensing experiments. Even through, an enhancement factor around 4 of the frequency shift is observed for the 60 nm particles. For smaller particles, the enhancement effect of the LSPR is further increased to 70× recently [72], however its sensitivity is still under the record in [1] due to the low quality factor.

Here, we improve the quality factor after coating metallic nanoparticles on the

cavity surface. Furthermore, we want this procedure to be repeatable and controllable. The first one that immediately comes out is the standard E-beam lithography. We use a dip coated PMMA layer as the resist. However, the resolution on the dielectric curved surface is low because of the strong charge effect. The focused ion beam (FIB) lithography shows the same situation. After the developing, metal coating and washing away the redundant PMMA and metal, the final cavity can not maintain the high quality factor. We believe that the last washing process leaves too much residues and kills the Q. The lithography is able to control the deposition position precisely, but the unavoidable washing approach is a big challenge for us.

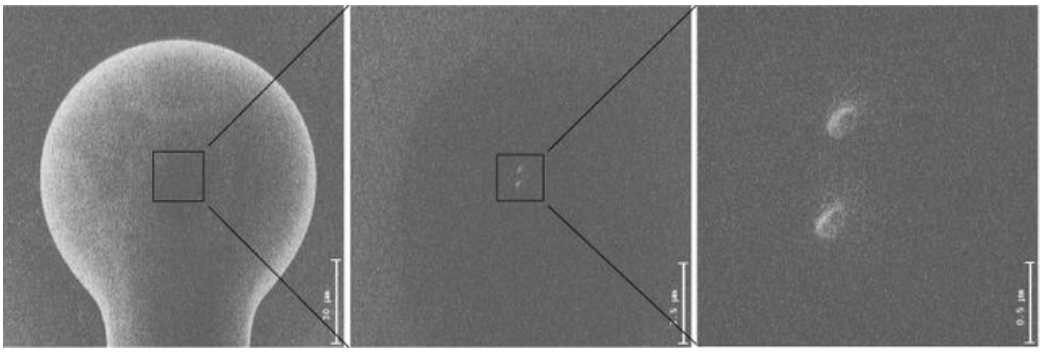

Figure 5.12: The FIB images of metallic nanodots on the spherical cavity surface. The diameter of the dots is around 50 nm and the distance between them is 500 nm.

One advantage of the FIB is that it can be used for direct deposition as well as the lithography [73]. Different from the lithography, one benefit of the direct deposition is the absence of resist during the fabrication. It makes the fabrication much more simple and easier, without the developing and washing processes. However, additional attentions need to be paid to the FIB deposition, since the charge effect has significant influence to the final quality of the deposited structure. First, the beam current should be as low as possible. The low current does result in the low image quality, but it greatly helps to weaken the charge effect. The well focused beam on the cavity surface is a prerequisite of the fabrication, which is hard to achieve with the strong charge effect. Secondly, the gallium ion in the beam is a contamination to the WGM cavity without the protection of PMMA resist. Even under the low current, a long exposing time to the ion beam leads to a notable dropping of the quality factor. Therefore, we should never underestimate the importance of adjusting the focus as quick as possible. The last key point that we find for the direct deposition is the dwell time. Experiments have shown the strong influence of the dwell time to the

formation of thin films [74]. A short dwell time is necessary for the good deposition quality, especially for the small structures.

In the FIB direct deposition, a tungsten tip is heated in front of the ion beam to produce the metallic vapor. Then, the atoms in the vapor are speeded up by the accelerated ions in the beam. When the working distance of the cavity sample is well aligned, the tungsten atoms are able to hit the cavity and form a structure on the surface according to the designed pattern. Fig. 5.12 shows the deposited pattern of two metallic dots. It is exactly the same as what we design. The two metallic dots with 50 nm diameter is located at both sides of the cavity equator, and the distance between them is set to be 500 nm. The measured quality factor of this cavity is above 2×10^7 in air. For the purpose of comparison, we put it into the real aqueous sensing environment and measure the Q with the reference interferometer at 630 nm. From the obtained spectrum in Fig. 5.13, we work out the Q of our spherical WGM cavity with metallic nanodots is $(1.4 \pm 0.1) \times 10^7$. This result is beyond one order better than other published results.

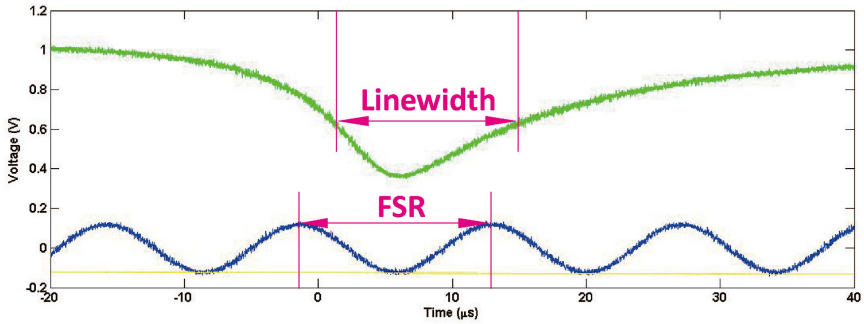

Figure 5.13: The output transmission of the microsphere with metallic nanodots. The FSR of the reference interferometer is 36 MHz and the Q is $(1.4 \pm 0.1) \times 10^7$.

5.5 Conclusion

We fabricate the high Q WGM cavities successfully with fused silica microsphere and microtoroid. The recorded ultra high Q is $(4.7 \pm 0.1) \times 10^8$ for the microsphere at 630 nm wavelength. Some unique phenomena for the ultra high Q ($Q > 10^8$) WGM cavities are observed, including the mode splitting. Based on the ultra high Q microspheres, we implement the metallic nanodots on the cavity surface with FIB for the first time. Meanwhile, the Q of the adorned WGM cavity is above 10^7 in both air

and water, which is over ten times better than the results published by other groups. One point we want to emphasize is that this new method is highly controllable and repeatable. It is easy to implement on other WGM cavities including the microtoroid.

This method opens a new field for the further investigation of the WGM cavity. Since the metallic dots on the cavity surface is highly controllable, we are able to modify the patterns from several different aspects. The easiest way is changing the size of the dots. When the size is small enough, the surface plasmon is not sensitive to the incident light angle. So it is easier for the excitation of the plasmon resonance. Besides, smaller metallic structure is helpful to keep the high Q of the WGM cavity, as the strong absorption of the light is from the metal. Secondly, we can adjust the distance between the dots and the positions as well. We already know that the light is circulating around the equator of the cavity. We can make the dots locate at such a position that the overlap of the dots and the mode pattern is optimized according to the mode profile. We want the amount of light is able to trigger the plasmon resonance in metal as little as possible. Too much light coupled into the metal is a waste but nothing. Next, the shape of the metallic pattern is also controllable by FIB. The simple dot is not necessarily a good candidate for the ultra high sensitive sensor. One can apply the nanoantenna technique to revise the plasmon mode pattern [75]. It is highly probable that the combing with optical nanoantenna expand the application of WGM sensing into a new area, such as high resolution bio-imaging [76]. As it is illustrated in Fig. 5.12, multiple dots on one single WGM cavity is doable. Hence, we are able to fabricate an array of metallic nanostructures. Based on the current research on nanoantenna arrays [77], it is also possible to realize the multiple sensing, optical trapping, stacking and sorting on a single WGM cavity.

Chapter 6

Summary

In this thesis, we present a new fabrication method to coat the whispering gallery microcavity with metallic nanostructures controllably. Furthermore a new mode solver for the silica microtoroid with very simple physics is presented.

We gave the basic physical principles of a WGM cavity at the very beginning. Some related important concepts are discussed, including the quality factor (Q), loss mechanisms and mode volume. The sensitivity of the WGM based senor is proportional to the Q and inversely proportional to its mode volume. Meanwhile, the Q is determined by the loss of a cavity. For our silica fused cavity, we talk in detail on how to reduce the intrinsic loss from surface scattering, contaminations, material absorption and radiation. From the comparison between microsphere and microtoroid, we know that the toroidal WGM cavity can confine the circulating light into a smaller volume than the sphere. With other features, we draw a conclusion that the microtoroid is a better platform for WGM sensing.

Besides the intrinsic quality factor, the coupling quality factor is another important parameter for the WGM sensing. It describes the coupling loss between a cavity and its coupler, which is used to couple light into the WGM and extract light for the measurement. We pay a lot of attention to the tapered fiber coupler and its coupling with the cavity. In order to offer a deep understanding of the coupling, we describe the coupling process mathematically and derive out the output transmission spectrum, resonant linewidth and buildup factor. It explains the theoretical principle of the Q measurement from the resonant linewidth and how the sensitivity is related to the Q of WGM cavities.

We also formulate a new mode solver for the toroidal WGM cavity and calculate the radiative quality factors based on the different mode solvers. As we known,

the microtoroid is better than the microsphere as a sensor. However, the current numerical mode solver for it is hard to understand. The physics behind our new mode solver is simple: expanding cavity modes to a set of straight fiber modes. Additionally, our modification is easy to transfer to any axial-symmetric WGM cavities. The radiation quality factors calculated from our new mode solver have a good agreement with that from the direct FEM toroid mode solver.

Finally, we successfully demonstrate the fabrication of high Q ($Q > 10^8$) silica microspheres and microtoroids by fusing silica with high power CO_2 laser. Based on the sensing principle of the WGM sensor and its current limitation, we show that the localized surface plasmon resonance (LSPR) is able to play a role in further improving the WGM sensitivity. We take the advantage of the focused ion beam (FIB) to fabricate a high Q spherical WGM cavity with two metallic nanodots near the equator. Its quality factor is $(1.4 \pm 0.1) \times 10^7$ in the aqueous environment, which is tens of times greater than the published results from other methods. Besides, its high controllability and repeatability offer an amount of opportunities to modify the metallic structure and plasmon patterns. This offers a new way for the further improvement of the WGM cavity based sensing and other useful applications such as optical capture.

Bibliography

[1] T. Lu, H. Lee, T. Chen, S. Herchak, J.-H. Kim, S. E. Fraser, R. C. Flagan, and K. Vahala, "High sensitivity nanoparticle detection using optical microcavities," *Proceedings of the National Academy of Sciences*, vol. 108, pp. 5976–5979, 2011.

[2] A. Yariv and P. Yeh, *Photonics. Optical Electronics in Modern Communications.* Ox, 6th ed., 2007.

[3] A. Matsko and V. Ilchenko, "Optical resonators with whispering-gallery modes-part i: basics," *Selected Topics in Quantum Electronics, IEEE Journal of*, vol. 12, pp. 3 – 14, jan.-feb. 2006.

[4] K. Vahala, "Optical microcavities," *NATURE*, vol. 424, pp. 839–846, AUG 14 2003.

[5] D. Armani, T. Kippenberg, S. Spillane, and K. Vahala, "Ultra-high-Q toroid microcavity on a chip," *NATURE*, vol. 421, pp. 925–928, FEB 27 2003.

[6] D. W. Vernooy, V. S. Ilchenko, H. Mabuchi, E. W. Streed, and H. J. Kimble, "High-q measurements of fused-silica microspheres in the near infrared," *Opt. Lett.*, vol. 23, pp. 247–249, Feb 1998.

[7] M. L. Gorodetsky, A. A. Savchenkov, and V. S. Ilchenko, "Ultimate q of optical microsphere resonators," *Opt. Lett.*, vol. 21, pp. 453–455, Apr 1996.

[8] M. Borselli, T. Johnson, and O. Painter, "Beyond the rayleigh scattering limit in high-q silicon microdisks: theory and experiment," *Opt. Express*, vol. 13, pp. 1515–1530, Mar 2005.

[9] D. J. Griffiths, *Introduction to Electrodynamics.* Prentice-Hall, 3rd ed., 1999.

[10] J. Homola, S. S. Yee, and G. Gauglitz, "Surface plasmon resonance sensors: review," *Sensors and Actuators B: Chemical*, vol. 54, no. 12, pp. 3 – 15, 1999.

[11] A. J. Benahmed and C.-M. Ho, "Bandgap-assisted surface-plasmon sensing," *Appl. Opt.*, vol. 46, pp. 3369–3375, Jun 2007.

[12] J. Homola, "Surface plasmon resonance sensors for detection of chemical and biological species," *Chem. Rev.*, vol. 108, no. 2, p. 462493, 2008.

[13] Y. H. Huang, H. P. Ho, S. Y. Wu, and S. K. Kong, "Detecting phase shifts in surface plasmon resonance: A review," *Advances in Optical Technologies*, vol. 2012, p. 471957, 2012.

[14] A. Ishimaru, S. Jaruwatanadilok, and Y. Kuga, "Generalized surface plasmon resonance sensors using metamaterials and negative index materials," *Progress In Electromagnetics Research*, vol. 51, pp. 139–152, 2005.

[15] F. Vollmer and S. Arnold, "Whispering-gallery-mode biosensing: label-free detection down to single molecules.," *Nature Methods*, vol. 5, no. 5, pp. 591–6, 2008.

[16] P. Stcker, B. Menges, U. Langbein, and S. Mittler, "Multimode waveguide mode surface plasmon coupling: a sensitivity and device realizability study," *Sensors and Actuators A: Physical*, vol. 116, no. 2, pp. 224 – 231, 2004.

[17] S. Shopova, C. Blackledge, and A. Rosenberger, "Enhanced evanescent coupling to whispering-gallery modes due togold nanorods grown on the microresonator surface," *Applied Physics B: Lasers and Optics*, vol. 93, pp. 183–187, 2008. 10.1007/s00340-008-3180-6.

[18] M. A. Santiago-Cordoba, S. V. Boriskina, F. Vollmer, and M. C. Demirel, "Nanoparticle-based protein detection by optical shift of a resonant microcavity," *Applied Physics Letters*, vol. 99, no. 7, p. 073701, 2011.

[19] S. I. Shopova, R. Rajmangal, S. Holler, and S. Arnold, "Plasmonic enhancement of a whispering-gallery-mode biosensor for single nanoparticle detection," *Applied Physics Letters*, vol. 98, no. 24, p. 243104, 2011.

[20] H. Yokoyama, "Physics and device applications of optical microcavities," *Science*, vol. 256, no. 5053, pp. 66–70, 1992.

[21] V. Ilchenko and A. Matsko, "Optical resonators with whispering-gallery modes-part ii: applications," *Selected Topics in Quantum Electronics, IEEE Journal of*, vol. 12, pp. 15 – 32, jan.-feb. 2006.

[22] L. Rayleigh, "The problem of the whispering gallery," *Scientific Papers (Cambridge Univ.)*, vol. 5, pp. 617–620, 1912.

[23] V. Braginsky, M. Gorodetsky, and V. Ilchenko, "Quality-factor and nonlinear properties of optical whispering-gallery modes," *Physics Letters A*, vol. 137, no. 78, pp. 393 – 397, 1989.

[24] X. Fan, I. M. White, S. I. Shopova, H. Zhu, J. D. Suter, and Y. Sun, "Sensitive optical biosensors for unlabeled targets: A review," *Analytica Chimica Acta*, vol. 620, no. 1-2, pp. 8 – 26, 2008.

[25] S. Arnold, R. Ramjit, D. Keng, V. Kolchenko, and I. Teraoka, "Microparticle photophysics illuminates viral bio-sensing," *Faraday Discuss.*, vol. 137, pp. 65–83, 2008.

[26] S. Arnold, D. Keng, S. I. Shopova, S. Holler, W. Zurawsky, and F. Vollmer, "Whispering gallery mode carousel – a photonic mechanism for enhanced nanoparticle detection in biosensing," *Opt. Express*, vol. 17, pp. 6230–6238, Apr 2009.

[27] L. Collot, V. Lefvre-Seguin, M. Brune, J. M. Raimond, and S. Haroche, "Very high- q whispering-gallery mode resonances observed on fused silica microspheres," *EPL (Europhysics Letters)*, vol. 23, no. 5, p. 327, 1993.

[28] D. W. Vernooy, A. Furusawa, N. P. Georgiades, V. S. Ilchenko, and H. J. Kimble, "Cavity qed with high-q whispering gallery modes," *Phys. Rev. A*, vol. 57, pp. R2293–R2296, Apr 1998.

[29] S. M. Spillane, T. J. Kippenberg, K. J. Vahala, K. W. Goh, E. Wilcut, and H. J. Kimble, "Ultrahigh-Q toroidal microresonators for cavity quantum electrodynamics," *Phys. Rev. A*, vol. 71, p. 013817, Jan 2005.

[30] G. Rempe, "Atoms in an optical cavity: Quantum electrodynamics in confined space," *Contemporary Physics*, vol. 34, no. 3, pp. 119–129, 1993.

[31] H. J. Kimble, "Strong interactions of single atoms and photons in cavity qed," *Physica Scripta*, vol. 1998, no. T76, p. 127, 1998.

[32] S. M. Spillane, T. J. Kippenberg, and K. J. Vahala, "Ultralow-threshold raman laser using a spherical dielectric microcavity," *Nature*, vol. 415, pp. 621–623, 2002.

[33] T. J. Kippenberg, S. M. Spillane, D. K. Armani, and K. J. Vahala, "Ultralow-threshold microcavity raman laser on a microelectronic chip," *Opt. Lett.*, vol. 29, pp. 1224–1226, Jun 2004.

[34] A. Ashkin and J. M. Dziedzic, "Observation of resonances in the radiation pressure on dielectric spheres," *Phys. Rev. Lett.*, vol. 38, pp. 1351–1354, Jun 1977.

[35] H. Lee, T. Chen, J. Li, K. Y. Yang, S. Jeon, O. Painter, and K. Vahala, "Chemically etched ultrahigh-Q wedge-resonator on a silicon chip," *Nat Photon*, vol. 6, pp. 369–373, 2012.

[36] R. Kitamura, L. Pilon, and M. Jonasz, "Optical constants of silica glass from extreme ultraviolet to far infrared at near room temperature," *Appl. Opt.*, vol. 46, pp. 8118–8133, Nov 2007.

[37] H. A. Haus, *Electromagnetic Noise and Quantum Optical Measurements*. Springer, 2000.

[38] J. D. Jackson, *Classical Electrodynamics*. Wiley, third edition ed., 1998.

[39] F. Vollmer, S. Arnold, and D. Keng, "Single virus detection from the reactive shift of a whispering-gallery mode," *Proceedings of the National Academy of Sciences*, vol. 105, no. 52, pp. 20701–20704, 2008.

[40] R. C. Smith and K. S. Baker, "Optical properties of the clearest natural waters (200–800 nm)," *Appl. Opt.*, vol. 20, pp. 177–184, Jan 1981.

[41] R. E. Hummel, *Electronic Properties of Materials*. Springer New York, fourth edition ed., 2011.

[42] B. Little, J.-P. Laine, and H. Haus, "Analytic theory of coupling from tapered fibers and half-blocks into microsphere resonators," *Lightwave Technology, Journal of*, vol. 17, pp. 704 –715, apr 1999.

[43] M. Oxborrow, "Traceable 2-D finite-element simulation of the whispering-gallery modes of axisymmetric electromagnetic resonators," *Microwave Theory and Techniques, IEEE Transactions on*, vol. 55, pp. 1209 –1218, june 2007.

[44] J. Vučković, M. Lončar, H. Mabuchi, and A. Scherer, "Design of photonic crystal microcavities for cavity qed," *Phys. Rev. E*, vol. 65, p. 016608, Dec 2001.

[45] H. Mabuchi and H. J. Kimble, "Atom galleries for whispering atoms: binding atoms in stable orbits around an optical resonator," *Opt. Lett.*, vol. 19, pp. 749–751, May 1994.

[46] M. Cai and K. Vahala, "Highly efficient optical power transfer to whispering-gallery modes by use of a symmetrical dual-coupling configuration," *Opt. Lett.*, vol. 25, pp. 260–262, Feb 2000.

[47] S. C. Hill and R. E. Benner, "Morphology-dependent resonances associated with stimulated processes in microspheres," *J. Opt. Soc. Am. B*, vol. 3, pp. 1509–1513, Nov 1986.

[48] M. Cai, O. Painter, K. J. Vahala, and P. C. Sercel, "Fiber-coupled microsphere laser," *Opt. Lett.*, vol. 25, pp. 1430–1432, Oct 2000.

[49] M. Cai, O. Painter, and K. J. Vahala, "Observation of critical coupling in a fiber taper to a silica-microsphere whispering-gallery mode system," *Phys. Rev. Lett.*, vol. 85, pp. 74–77, Jul 2000.

[50] J. C. Knight, G. Cheung, F. Jacques, and T. A. Birks, "Phase-matched excitation of whispering-gallery-mode resonances by a fiber taper," *Opt. Lett.*, vol. 22, pp. 1129–1131, Aug 1997.

[51] S. P. Vyatchanin, M. L. Gorodetskii, and V. S. Il'chenko, "Tunable narrow-band optical filters with modes of the whispering gallery type," *Journal of Applied Spectroscopy*, vol. 56, pp. 182–187, 1992. 10.1007/BF00662275.

[52] M. Gorodetsky and V. Ilchenko, "High-Q optical whispering-gallery microresonators: precession approach for spherical mode analysis and emission patterns with prism couplers," *Optics Communications*, vol. 113, no. 13, pp. 133 – 143, 1994.

[53] A. Serpengüzel, S. Arnold, and G. Griffel, "Excitation of resonances of microspheres on an optical fiber," *Opt. Lett.*, vol. 20, pp. 654–656, Apr 1995.

[54] G. Griffel, S. Arnold, D. Taskent, A. Serpengüzel, J. Connolly, and N. Morris, "Morphology-dependent resonances of a microsphere-optical fiber system," *Opt. Lett.*, vol. 21, pp. 695–697, May 1996.

[55] N. Dubreuil, J. C. Knight, D. K. Leventhal, V. Sandoghdar, J. Hare, and V. Lefèvre, "Eroded monomode optical fiber for whispering-gallery mode excitation in fused-silica microspheres," *Opt. Lett.*, vol. 20, pp. 813–815, Apr 1995.

[56] G. Keiser, *Optical Fiber Communications*. McGraw-Hill, Inc., 2nd ed., 1991.

[57] S. M. Spillane, T. J. Kippenberg, O. J. Painter, and K. J. Vahala, "Ideality in a fiber-taper-coupled microresonator system for application to cavity quantum electrodynamics," *Phys. Rev. Lett.*, vol. 91, p. 043902, July 2003.

[58] D. Gloge, "Weakly guiding fibers," *Appl. Opt.*, vol. 10, pp. 2252–2258, Oct 1971.

[59] M. L. Gorodetsky and V. S. Ilchenko, "Optical microsphere resonators: optimal coupling to high-q whispering-gallery modes," *J. Opt. Soc. Am. B*, vol. 16, pp. 147–154, Jan 1999.

[60] B. Min, L. Yang, and K. Vahala, "Perturbative analytic theory of an ultrahigh-Q toroidal microcavity," *Phys. Rev. A*, vol. 76, p. 013823, Jul 2007.

[61] D. Marcuse, "Curvature loss formula for optical fibers," *J. Opt. Soc. Am.*, vol. 66, pp. 216–220, Mar 1976.

[62] A. W. Snyder and J. D. Love, *Optical Waveguide Theory*. Chapman and Hall, 1st ed., 1983.

[63] R. Schermer and J. Cole, "Improved bend loss formula verified for optical fiber by simulation and experiment," *Quantum Electronics, IEEE Journal of*, vol. 43, pp. 899 –909, oct. 2007.

[64] A. Melloni, F. Carniel, R. Costa, and M. Martinelli, "Determination of bend mode characteristics in dielectric waveguides," *J. Lightwave Technol.*, vol. 19, p. 571, Apr 2001.

[65] A. Ashkin, J. M. Dziedzic, J. E. Bjorkholm, and S. Chu, "Observation of a single-beam gradient force optical trap for dielectric particles," *Opt. Lett.*, vol. 11, pp. 288–290, May 1986.

[66] A. Ashkin, "History of optical trapping and manipulation of small-neutral particle, atoms, and molecules," *Selected Topics in Quantum Electronics, IEEE Journal of*, vol. 6, pp. 841 –856, nov/dec 2000.

[67] S. Chu, J. E. Bjorkholm, A. Ashkin, and A. Cable, "Experimental observation of optically trapped atoms," *Phys. Rev. Lett.*, vol. 57, pp. 314–317, Jul 1986.

[68] A. Ashkin and J. Dziedzic, "Optical trapping and manipulation of viruses and bacteria," *Science*, vol. 235, no. 4795, pp. 1517–1520, 1987.

[69] T. Kippenberg, "Microresonators: Particle sizing by mode splitting," *Nature Photonics*, vol. 4, pp. 9–10, 2010.

[70] J. D. Swaim, J. Knittel, and W. P. Bowen, "Detection limits in whispering gallery biosensors with plasmonic enhancement," *Applied Physics Letters*, vol. 99, no. 24, p. 243109, 2011.

[71] S. I. Shopova, C. W. Blackledge, A. T. Rosenberger, and N. F. Materer, "Gold nanorods grown from hgte nanoparticles directly on various surfaces," *Applied Physics Letters*, vol. 89, no. 2, p. 023120, 2006.

[72] V. R. Dantham, S. Holler, V. Kolchenko, Z. Wan, and S. Arnold, "Taking whispering gallery-mode single virus detection and sizing to the limit," *Applied Physics Letters*, vol. 101, no. 4, p. 043704, 2012.

[73] K. Gamo, "Nanofabrication by fib," *Microelectronic Engineering*, vol. 32, no. 14, pp. 159 – 171, 1996.

[74] S. Hausmann, L. Bischoff, J. Teichert, D. Grambole, F. Herrmann, and W. Mller, "Investigation of dwell-time effects on the cobalt disilicide formation using focused ion beam implantation," *Microelectronic Engineering*, vol. 4142, no. 0, pp. 233 – 236, 1998.

[75] T.-R. Lin, S.-W. Chang, S. L. Chuang, Z. Zhang, and P. J. Schuck, "Coating effect on optical resonance of plasmonic nanobowtie antenna," *Applied Physics Letters*, vol. 97, no. 6, p. 063106, 2010.

[76] L. Zhou, Q. Gan, F. J. Bartoli, and V. Dierolf, "Direct near-field optical imaging of uv bowtie nanoantennas," *Opt. Express*, vol. 17, pp. 20301–20306, Oct 2009.

[77] B. J. Roxworthy, K. D. Ko, A. Kumar, K. H. Fung, E. K. C. Chow, G. L. Liu, N. X. Fang, and K. C. Toussaint, "Application of plasmonic bowtie nanoantenna arrays for optical trapping, stacking, and sorting," *Nano Letters*, vol. 12, no. 2, pp. 796–801, 2012.

Appendix A

Appendix

A.1 Vector Identity

Use the index notation and Einstein Summation Convention,

$$\delta_{ij} = \begin{cases} 1 & \text{if} \quad i = j \\ 0 & \text{otherwise} \end{cases} \tag{A.1}$$

and

$$\varepsilon_{ijk} = \begin{cases} +1 & \text{if} \quad ijk = 123, 312, \ or \ 231 \\ -1 & \text{if} \quad ijk = 132, 321, \ or \ 213 \\ 0 & \text{otherwise} \end{cases} \tag{A.2}$$

and an useful identity

$$\varepsilon_{ijk}\varepsilon_{ilm} = \delta_{jl}\delta_{km} - \delta_{jm}\delta_{kl}. \tag{A.3}$$

The dot product of two vectors $\mathbf{A} \cdot \mathbf{B}$ in this notation is

$$\begin{aligned} \mathbf{A} \cdot \mathbf{B} &= A_1B_1 + A_2B_2 + A_3B_3 = \sum_{i=1}^{3} A_iB_i \\ &= \sum_{i=1}^{3}\sum_{j=1}^{3} A_iB_j\delta_{ij} = A_iB_i. \end{aligned} \tag{A.4}$$

The i^{th} component of the cross product of two vectors becomes

$$(\mathbf{A} \times \mathbf{B})_i = \sum_{j=1}^{3} \sum_{k=1}^{3} A_j B_k = \varepsilon_{ijk} A_j B_k. \tag{A.5}$$

So,

$$\begin{aligned} (\nabla \times (\nabla \times \mathbf{A}))_i &= \varepsilon_{ijk} \partial_j (\nabla \times \mathbf{A}) \\ &= \varepsilon_{ijk} \partial_j \varepsilon_{klm} \partial_l A_m \\ &= \varepsilon_{ijk} \varepsilon_{klm} \partial_j \partial_l A_m \\ &= (\delta_{il}\delta_{jm} - \delta_{im}\delta_{jl}) \partial_j \partial_l A_m \\ &= \partial_i (\partial_j A_j) - \partial_j \partial_j A_i \\ &= \partial_i (\nabla \cdot \mathbf{A}) - \nabla^2 A_i. \end{aligned} \tag{A.6}$$

Finally,

$$\nabla \times (\nabla \times \mathbf{A}) = \nabla(\nabla \cdot \mathbf{A}) - \nabla^2 \mathbf{A}. \tag{A.7}$$

A.2 Material Loss Simulation

The principle of the simulation for the α_{eff} is as the following:

Assume that the refractive index of the cavity and environment hybrid system is $n(r,z,\phi) = n(r,z)$, and the field propagating after a small angle $d\phi$ is

$$E(r,z,\phi+d\phi) = E(r,z,\phi)e^{j\frac{2\pi nr\Delta\phi}{\lambda}-\frac{r\Delta\phi\alpha}{2}}. \tag{A.8}$$

So the power is

$$\begin{aligned} & P(\phi+d\phi) \\ = \quad & c\epsilon_0 \int n(r,z)E^*(r,z,\phi+d\phi)E(r,z,\phi+d\phi)drdz \\ = \quad & P(\phi)e^{-\overline{r\alpha}\Delta\phi}. \end{aligned} \tag{A.9}$$

This leads to

$$\begin{aligned} e^{-\overline{r\alpha}\Delta\phi} &= \frac{P(\phi+d\phi)}{P(\phi)} \\ &= \frac{\int n(r,z)e^{-r\Delta\phi\alpha(r,z)}E^*(r,z)E(r,z)drdz}{\int n(r,z)E^*(r,z)E(r,z)drdz} \\ &= \frac{<E|ne^{-r\Delta\phi\alpha}|E>}{<E|n|E>}. \end{aligned} \tag{A.10}$$

Therefore,

$$\overline{\alpha} = -\frac{1}{\overline{r}\Delta\phi} ln \frac{<E|ne^{-r\Delta\phi\alpha}|E>}{<E|n|E>}, \tag{A.11}$$

$$\overline{r} = \frac{<E|nr|E>}{<E|n|E>}. \tag{A.12}$$

As $r\Delta\phi\alpha \ll 1$,

$$\begin{aligned}
\overline{\alpha} &= -\frac{1}{\overline{r}\Delta\phi} ln[1 - \frac{< E|nr\Delta\phi\alpha|E >}{< E|n|E >}] \\
&\simeq \frac{1}{\overline{r}\Delta\phi} \frac{< E|nr\alpha|E >}{< E|n|E >} \Delta\phi \\
&= \frac{< E|nr\alpha|E >}{< E|nr|E >} \\
&= \frac{\int n(r,z)\alpha(r,z) r E^*(r,z) E(r,z) dr dz}{\int n(r,z) r E^*(r,z) E(r,z) dr dz} \\
&= \alpha_{eff}.
\end{aligned} \tag{A.13}$$

A.3 Perturbation Theory

The electric field in a cavity obeys the Helmhöltz equation,

$$\nabla^2\mathbf{E} + \frac{1}{c^2}\epsilon_r\omega_0^2\mathbf{E} = 0. \tag{A.14}$$

When a particle with a small volume V_p is attached to the cavity, it changes the field distribution slightly due to its different relative permittivity $\epsilon_p = \epsilon_r + \delta\epsilon_r$ to the environment. Since its small size compared with the cavity, we consider the change as a perturbation to the first order that $\mathbf{E}' = \mathbf{E} + \delta\mathbf{E}$ and $\omega_0' = \omega_0 + \delta\omega$ [37]. Then, the Helmhöltz equation still holds,

$$\nabla^2(\mathbf{E} + \delta\mathbf{E}) + \frac{1}{c^2}(\epsilon_r + \delta\epsilon_r)(\omega_0 + \delta\omega)^2(\mathbf{E} + \delta\mathbf{E}) = 0. \tag{A.15}$$

Expanding this equation and ignoring the high order perturbation terms, it yields

$$\nabla^2\mathbf{E} + \nabla^2\delta\mathbf{E} + \frac{1}{c^2}\epsilon_r\omega_0^2\mathbf{E} + \frac{1}{c^2}\epsilon_r\omega_0^2\delta\mathbf{E} + \frac{1}{c^2}(\omega_0^2\delta\epsilon_r + 2\epsilon_r\omega_0\delta\omega)\mathbf{E} = 0. \tag{A.16}$$

Combining with Eq. (A.14), we obtain

$$\nabla^2\delta\mathbf{E} + \frac{1}{c^2}\epsilon_r\omega_0^2\delta\mathbf{E} + \frac{1}{c^2}(\omega_0^2\delta\epsilon_r + 2\epsilon_r\omega_0\delta\omega)\mathbf{E} = 0. \tag{A.17}$$

Dot multiply the complex conjugate of Eq. (A.14) by $\delta\mathbf{E}$ and Eq. (A.17) by $\mathbf{E}^*$, we have

$$\delta\mathbf{E}\nabla^2\mathbf{E}^* + \frac{1}{c^2}\epsilon_r\omega_0^2\delta\mathbf{E}\mathbf{E}^* = 0 \tag{A.18}$$

and

$$\mathbf{E}^*\nabla^2\delta\mathbf{E} + \frac{1}{c^2}\epsilon_r\omega_0^2\delta\mathbf{E}\mathbf{E}^* + \frac{1}{c^2}(\omega_0^2\delta\epsilon_r + 2\epsilon_r\omega_0\delta\omega)\mathbf{E}\mathbf{E}^* = 0. \tag{A.19}$$

Then, subtracting them and after some rearranging, we arrive at the following integral expression over the whole space

$$\int(\omega_0\delta\epsilon_r + 2\epsilon_r\delta\omega)\mathbf{E}\mathbf{E}^* dV = 0 \tag{A.20}$$

Solving it for $\delta\omega$, we find

$$\delta\omega = -\omega_0\frac{\int\delta\epsilon_r|\mathbf{E}|^2 dV}{2\int\epsilon_r|\mathbf{E}|^2 dV}. \tag{A.21}$$

When the particle is much smaller than the wavelength, we can ignore the field varying around the particle and assume that it is fixed in a plane wave field $\mathbf{E}(\mathbf{r})$ localized at the particle position in stead of an evanescent field. This yields

$$\delta\omega = -\omega_0 \frac{\delta\epsilon_r |\mathbf{E}(\mathbf{r})|^2 V_p}{2\int \epsilon_r |\mathbf{E}|^2 dV}. \tag{A.22}$$